3.2.1 Number of papers published per teacher in the Journals notified on UGC website during the year

ACADEMIC YEAR 2023-2024

S.NO	Author Name	Title of the Papers	Journal Name	Publisher	Year
1.	Ommurugadhasan D	Electric Discharge Machining of Aluminium Silicon-Carbide Composite and Optimization of Process Parameters	ES Materials and Manufacturing	Engineered Science Publisher	**2024**
2.	Anita Sebasthiyar	Modified Exigent Features Block in JAN Net for Analysing SPECT Scan Images to Diagnose Early-Stage Parkinson's Disease	Current Medical Imaging	Bentham Science Publisher	**2024**

ES Materials and Manufacturing
DOI: https://dx.doi.org/10.30919/esmm1076

Electric Discharge Machining of Aluminium Silicon-Carbide Composite and Optimization of Process Parameters

Harinesh B,[1] Arunachalam U,[2] Ommurugadhasan D[3] and Jenarthanan M. P.[1,*]

Abstract

Aluminium metal matrix composites are hard to machine due to the bonding properties of the base and the reinforced ceramic materials. Electric discharge machining is one of the common and effective methods for machining such materials. The present work is to study the effect of pulse duration, peak current and the electrode gap on metal removal rate (MRR), tool wear ratio (TWR) and radial over cut (ROC) on electric discharge machining of aluminium silicon carbide composites of various compositions 3%, 6% and 9%. The experiment was carried out using copper electrode of 3.4 mm diameter. Taguchi L_9 orthogonal array was considered for analysing the results. Statistical models based on experiments are used for optimising the parameters for electric discharge machining (EDM) for this experiment.

Keywords: Aluminium matrix composites; EDM; Optimization; Taguchi technique.
Received: 18 August 2023; Revised: 14 December 2023; Accepted: 22 December 2023.
Article type: Research article.

1. Introduction

A composite material (also called a composition material or shortened to composite) is a material made from two or more constituent materials with significantly different physical or chemical properties that, when combined, produce a material with characteristics different from the individual components. The individual components remain separate and distinct within the finished structure. The new material may be preferred for many reasons: common examples include materials which are stronger, lighter, or less expensive when compared to traditional materials. The increasing demand for new, lightweight materials with greater strength and toughness has led to the development of a new generation of composite materials over the last decade, even though these same properties create major challenges for machining.

Whilst possessing a greater hardness and reinforcement strength, composite materials cause serious tool flank wear when using traditional techniques. However, advanced non-traditional machining techniques such as water jet machining, laser machining and wire electrical discharge machining (WEDM) can be applied, mainly in linear cutting. The intrinsic designation of these techniques limits their application to blind-hole machining. Thus, EDM becomes an optimal choice in the machining of a blind-hole workpiece owing to its easy control in operation and precise criterion of high complex-shape demand. The merits of the electrical discharge machining (EDM) technique become most apparent in the machining of MMC, which has the highest hardness in reinforcement.

The metal matrix composites offer higher modulus of elasticity, ductility and resistance to elevated temperature than polymer matrix composites. But, they are heavier and more difficult to process. EDM is a well-established machining option for manufacturing geometrically complex or hard material parts that are extremely difficult to machine by conventional machining processes. The non-contact machining technique has been continuously evolving from a mere tool and dies making process to a micro-scale application machining alternative attracting a significant amount of research interest. In recent years, EDM researchers have explored many ways to improve the sparking efficiency including some unique experimental concepts that depart from the EDM traditional sparking phenomenon. Despite a range of different approaches, this new research shares the same objectives of achieving more efficient metal removal coupled with a reduction in tool wear and improved surface quality.

EDM process was to minimize the damage caused in steel and inferred the process parameters like MRR and average arithmetic mean of surface roughness.[1-8] Taguchi$_{27}$ orthogonal array was utilized. The ANOVA demonstrated that the most influential parameter for improved performance is the speed. Optimising the machining parameters of EDM on aluminium oxide (Al_2O_3) ceramics using Taguchi based on

[1] *School of Mechanical Engineering, SASTRA Deemed University, Thanjavur 613401, Tamilnadu, India.*
[2] *Department of Mechanical Engineering, University College of Engineering, Nagercoil 629004, Tamilnadu, India.*
**Email:* jenarthanan@mech.sastra.edu (Jenarthanan M. P.)

TOPSIS coupled with the AHP weight method.[9-11] The study states that the adhesive foil of Al_2O_3 ceramics had a significant impact on MRR, electrode removal rate and surface roughness. And also states that this approach might be utilized to improve and optimize additional process parameters.

Material Removal Rate (MRR), Surface Roughness (SR), and the micro-hardness of a machined surface (HV) in electrical discharge machining of die steels in dielectric fluid with mixed powder were optimized simultaneously using the Taguchi–TOPSIS method.[12-14] The process parameters used in the study included workpiece materials (SKD61, SKD11, SKT4), electrode materials (copper, graphite), electrode polarity, pulse-on time, pulse-off time, current, and titanium powder concentration.

The dielectric fluid plays a significant role in the characteristics of the machining process such as Tool Wear Rate (TWR), Material Removal Rate (MRR) and more.[15] Conventional dielectric fluids have disadvantages they emit carbon dioxide, carbon monoxide gases in the environment. Vegetable based bio-oil/ biodiesels are biodegradable, environment friendly and they emit less harmful gases. In this paper study of various waste vegetable oils used as dielectric fluid is considered and the overall effect on the EDM is analysed. Relevant literature on EDM and the impact of process parameters on performance measures such as surface quality, tool wear rate and material removal rate are reviewed.[7] The challenges and limitations of EDM process are also highlighted in this article. It is observed that optimization of process parameters is essentially required for effective and economical machining.

The feasibility of using the non-conventional EDM process for MMCs was confirmed, and models based on two-level factorial experiments were developed.[4] Although further study is necessary to investigate the validity of the models in different ranges, and to find the global optimum parameters, the results of this study in these experimental ranges suggested that: The SiC particles shield the aluminium alloy matrix from being eroded by the EDM sparks. Lower metal removal rate therefore results for MMCs with higher particle percentages. The unavoidable RCL was formed mainly due to inadequate flushing by the dielectric. Softened fine grains containing irregular voids, spherical bubbles, and high particle density are characteristics of the RCL. Such layer should be removed when an EDMed MMC component is used in a critical application. Severe sub-surface damage due to abnormal arcing was observed when EDM AI-20v% SiCp at high power and high frequency settings. The thin and softened HAZ is difficult to see. Solution heat treatment prior to EDM, special etchant to enhance the precipitates, and transmission electron microscopy could be used to verify the existence of such HAZ. The power level (voltage × current) dominates all other factors and greatly effects the MRR, and the RCL. The current alone, however, controls the surface finish. Due to its modest MRR, EDM should only be chosen over a conventional process to form complex or very small size features.

The introduction of EDM to metal cutting has been a viable machining option of producing highly complex parts, independent of the mechanical properties of workpiece material.[5] This is by the capability of EDM to economically machine parts, which are difficult to be carried out by conventional material removal processes. With continuous improvement in the metal removal efficiency and the incorporation of numerical control, the viability of the EDM process in terms of the type of applications can be considerably extended. The basis of controlling the EDM process mostly relies on empirical methods largely due to the stochastic nature of the sparking phenomenon involving both electrical and non-electrical process parameters. The complicated interrelationship between the different optimised process parameters is therefore a major factor contributing to the overall machining efficiency. However, several means of improving the machining performance commonly measured in terms of MRR, TWR and SR have been made with an overwhelming research interest being paid to the metallurgical properties of the EDMed part. Thus, the EDM process needs to be constantly revitalised to remain competitive in providing an essential and valuable role in the tool room manufacturing of parts with difficult-to-machine materials and geometries.

The feasibility of machining Al–10% SiCp MMCs. MRR was found to be higher for larger current and pulse on-time settings at the expense of taper city, radial overcut and surface finish. TWR was also found to be higher, larger than the MRR, for larger current settings.[10] At higher current and ON-time ratings, the dimensional accuracy is affected. Flushing pressure of the dielectric has a considerable effect on the MRR and TWR. The Taguchi L_9 orthogonal array with Grey relational analysis was employed to optimize the multi response characteristics of Electric Discharge Machining of Al–10%SiCP composites.[10] The experimental result for the optimal setting shows that there is considerable improvement in the process. The application of this technique converts the multi response variable to a single response Grey relational grade and, therefore, simplifies the optimization procedure.

The feasibility of machining Al–SiC composites by EDM drilling with tube electrodes has been evaluated. From the results of this experiment, the following conclusions can be drawn. The effect of EDM drilling with the rotating tube electrode has produced a higher material removal rate than the rotating solid electrode. The electrode tube hole diameter significantly affects the MRR, EWR and SR. The decrease in hole diameter has produced a better MRR, SR and higher EWR. The increase in the volume percentage of SiC has resulted in a decrease in MRR, SR and an increase in EWR. The increase in rotational speed of the tube electrode has produced higher MRR, EWR and better SR. The MRR, EWR was more for the injection flushing than the side flushing.[13]

The Material Removal Rate (MRR) increases with an increase in the peak current irrespective concentration of silicon carbide in the aluminium metal matrix composite.[16-20] The MRR for 9% concentration of silicon carbide in aluminium is the lowest irrespective of the peak current and powder concentration in dielectric fluid. At lower peak current (2A), the MRR increases with the increase in the aluminium powder concentration in the dielectric fluid up to a certain limit. Aluminium alloy-silicon carbide composites were developed using the vortex method and pressure die casting

technique.[22,23] The EDM studies showed that the MRR and the surface roughness are greatly influenced by the current and percent weight silicon carbide. The MRR increases with an increase in the current and decrease in the percent weight of silicon carbide. The surface finish improves with decrease in the current and increase in the percent weight of silicon carbide. An experimental study was carried to investigate the influence of three conductive powders: zinc, cobalt, and molybdenum, while machining Nimonic 75, a nickel-based superalloy, by the EDM process.[24,25] The work material considered in the study has been widely used in the aerospace industries and in applications involving higher temperatures. The experiments were carried out based on the Response Surface Methodology using the Box–Behnken design. Using the experimental data, regression equations were formed to predict the outcome of the process, which are Material Removal Rate (MRR), Electrode Wear Ratio (EWR), and Surface Roughness (SR). In this research machinability of Aluminium Silicon Carbide composites using conventional machining methods and comparison the results with the un-conventional machining method (EDM) were performed. This research also evaluates the feasibility of electric discharge machining of Al-3% SiC, Al-6% SiC and Al-9% SiC composites.

2. Materials and method

Aluminium is a relatively soft, durable, lightweight, ductile and malleable metal with appearance ranging from silvery to dull grey, depending on the surface roughness. It is nonmagnetic and does not easily ignite. A fresh film of aluminium serves as a good reflector (approximately 92%) of visible light and an excellent reflector (as much as 98%) of medium and far infrared radiation. The yield strength of pure aluminium is 7–11 MPa, while aluminium alloys have yield strengths ranging from 200 MPa to 600 MPa. Aluminium has about one-third the density and stiffness of steel. It is easily machined, cast, drawn and extruded. Aluminium atoms are arranged in a Face-Centered Cubic (FCC) structure. Aluminium in bar form was procured.

Grains of silicon carbide can be bonded together by sintering to form very hard ceramics that are widely used in applications requiring high endurance, such as car brakes, car clutches and ceramic plates in bulletproof vests. Electronic applications of silicon carbide as light-emitting diodes (LEDs) and detectors in early radios were first demonstrated around 1907. SiC is used in semiconductor electronics devices that operate at high temperatures or high voltages or both. Silicon Carbide was procured in powder form.

For manufacturing of composite material using stir casting process- various process parameters if they properly controlled can lead to improved characteristics in composite material such as Stirring speed, Stirring temperature, Reinforcement preheat temperature, Stirring time, Blade Angle, Inert Gas, Preheated Temperature of Mould Powder and Feed Rate.

2.1 Fabrication of MMC

A conical shaped graphite crucible is used for fabrication of AMCs, as it withstands high temperatures which is much more than the required temperature [680 °C]. Along that graphite will not react with aluminium at this temperature. This crucible is placed in muffle which is made up of high ceramic alumina. Around which the heating element was wound. The coil which acts as heating element is Kanthol-A1. This type of furnace is known as resistance heating furnace. It can work up to 900 °C reach within 45 min. Aluminium, at liquid stage is very reactive with atmospheric oxygen. Oxide formation occurs when it comes in contact with the open air. Thus, all the process of stirring is carried out in closed chamber with nitrogen gas as inert gas to avoid oxidation. Closed chamber is formed with help of steel sheet. This reduces heat loss and gas transfer as compared open chamber. A K type Temperature thermocouple whose working range is -200 °C to 1250 °C is used to record the current temperature of the liquid.

Due to corrosion resistance to atmosphere EN 24 is selected as stirrer shaft material. One end of shaft is connected to 0.5 hp PMDC motor with flange coupling. While at the other end blades are welded. 4 blades are welded to the shaft at 45 °C. A constant feeding rate of reinforcement particles is required to avoid coagulation and segregation of the particles. This can be achieve by using hopper. Aluminium matrix will be formed in the crucible by heating aluminium ingots in furnace. A stirring action is started at slow rate of 30 rpm and increases slowly in between 300 to 600 rpm with speed controller. A mixture of reinforcements (Al+ SiC) is to be incorporated in the metal matrix at semisolid level near 640 °C. Dispersion time is to be taken as 5 minutes. After that slurry is reheated to a temperature above melting point to make sure slurry is fully liquid and then it is poured in mould.

Stir casting process starts with placing empty crucible in the muffle. At first heater temperature is set to 500 °C and then it is gradually increased up to 900 °C Aluminium is used as Matrix material. Required quantity of aluminium is cut from the raw material which is in the form of round bar. Aluminium is cleaned to remove dust particles, weighed and then poured in the crucible for melting. During melting nitrogen gas is used as inert gas to create the inert atmosphere around the molten matrix. Powder of aluminium (Al), silicon carbide (SiC) and graphite are used as reinforcement. 1% by weight of pure magnesium powder is used as wetting agent. At a time total 700 gram of molten composite was processed in the crucible. Required quantities of reinforcement powder and magnesium powder are weighed on the weighing machine. Then it is thoroughly mixed with each other with the help of blending machine for 24 hour. This mixture is kept ready 1 day before the test has to carry out. Prior to conducting the test this mixture is kept for heating in another heater.

Reinforcements are heated for half hour and at temperature of 500 °C. When matrix was in the fully molten condition, Stirring is started after 2 minutes. Stirrer rpm is gradually increased from 0 to 300 rpm with the help of speed controller. The temperature of the heater is set to 630 °C which is below the melting temperature of the matrix. A uniform semisolid stage of the molten matrix was achieved by stirring it at 630 °C. Pouring of preheated reinforcements at the semisolid stage of the matrix enhances the wettability of the reinforcement,

reduces the particle settling at the bottom of the crucible. Reinforcements are poured manually with the help of conical hopper. The flow rate of reinforcements measured was 0.5 gram per second. Dispersion time was taken as 5 minutes. After stirring 5 minutes at semisolid stage slurry was reheated and hold at a temperature 900 °C to make sure slurry was fully liquid. Stirrer rpm was then gradually lowered to the zero. The stir casting apparatus is manually kept side and then molten composite slurry is poured in the metallic mould. Mould is preheated at temperature 500 °C before pouring of the molten slurry in the mould. This makes sure that slurry is in molten condition throughout the pouring. While pouring the slurry in the mould the flow of the slurry is kept uniform to avoid trapping of gas. Finally quenching is performed with the help of pressurized air to reduce the settling time of the particles in the matrix.

2.2 Testing

Hardness and Tensile test (Fig. S1) was carried out as per the ASTM standards and their results were obtained.

2.3 EDM set-up

Die sinking EDM machine is used to perform the machining operations. The machine has a tank dimension of "700 mm × 500 mm × 350 mm", as a result it needs large amount of aluminium powder to contaminate the dielectric fluid in the tank to get desired concentration for the experimentation and it also leads to usage of more dielectric fluid for the experimentation, moreover the usage of filtering techniques would also increase difficulties in conducting experimentation (Fig. 1). So, to overcome these difficulties a new tank, having volume of 7 litres with incorporated work holding device, has been chosen for conducting experimentation. For proper blending of aluminium powder with dielectric fluid and circulating the same in the spark gap, a special and portable electric pump is fixed with the EDM machine. This setup used for performing experimentation is shown.

Aluminium reinforced with three different percentages of SiC 3%, 6% and 9%) is used as work piece materials and these work pieces are fabricated by 'stir casting method'. The tool electrode used for machining is copper rod having 47.48 mm diameter. Aluminium powders with various concentrations are blended with dielectric fluid for the experimentation.

A random experiment is conducted to ascertain few fixed parameters and to find out the range of the process parameters to be used in the experimentations, these parameters are shown in the Table 1.

After fixing the process parameters, experiments are designed on the basis of "FACE CENTERED CENTRAL COMPOSITE DESIGN". This FCCCD comprises three level factorial points and star points at the centre of each.

2.4 Design of experiments

Considering Taguchi L_9 Orthogonal array, three parameters were considered (Table 2).

Table 1. Parameters and their range.

Parameters	Minimum Range	Moderate Range	Maximum Range
Pulse On/Off (μs)	2/4	4/6	6/8
Peak Current (A)	1.5	2.5	3.5
Electrode Gap (Mm)	5	5.5	6

Table 2. L_9 orthogonal array table.

Trial	Parameter 1	Parameter 2	Parameter 3
1	1	1	3
2	1	2	2
3	1	3	1
4	2	1	2
5	2	2	1
6	2	3	3
7	3	1	1
8	3	2	3
9	3	3	2

2.5 Tool selection

Copper electrode was selected of length 47.48mm and diameter 3.4mm (Fig. S3).

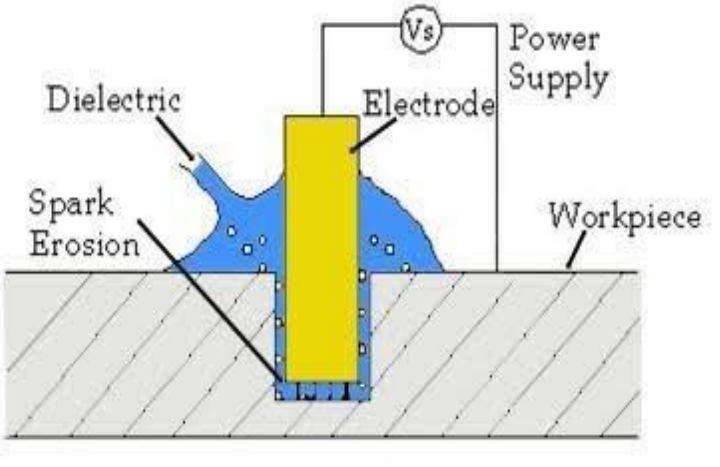

Fig. 1 Diagrammatic representation of EDM.

2.6 Evaluation of response variables

MRR is expressed as the ratio of the difference of weight of work piece before and after machining to that of the machining time:

$$\text{MRR} = \frac{\text{Weight loss of the work material}}{\text{Density of work material x time}} (\text{mm}^3/\text{min}) \quad (1)$$

TWR is expressed ad the ratio of difference of weight of the tool before and after machining to that of the machining time:

$$\text{TWR} = \frac{\text{Weight loss of the tool electrode}}{\text{Density of toolmaterial X time}} (\text{mm}^3/\text{min}) \quad (2)$$

Radial over cut (ROC) is expressed as half the difference of the diameter of the hole produced to the tool diameter:

$$ROC = \frac{d_{p-d_t}}{2} \ \ldots\ldots\ldots \ (\text{mm}) \quad (3)$$

where d_p the diameter of the hole drilled is, d_t is the diameter of the tool. The influence of Al-SiC percentage on outputs is as shown in Tables 3-5.

Table 3. Taguchi L_9 experimental runs for Al-SiC 3%.

Trial no.	Pulse on (µs)	Peak current (A)	Electrode gap (mm)	MRR (mm³/min)	TWR (mm)	ROC (mm)
1	2	1.5	6.0	104.90	0.023	0.005
2	2	2.5	5.5	125.19	0.024	0.015
3	2	3.5	5.0	135.19	0.026	0.015
4	4	1.5	5.5	125.18	0.023	0.025
5	4	2.5	5.0	135.19	0.025	0.030
6	4	3.5	6.0	146.93	0.027	0.025
7	6	1.5	5.0	129.97	0.025	0.035
8	6	2.5	6.0	140.79	0.027	0.045
9	6	3.5	5.5	146.91	0.029	0.050

Table 4. Taguchi L_9 experimental runs for Al-SiC 6%.

Trial no.	Pulse on (µs)	Peak current (A)	Electrode gap (mm)	MRR (mm³/min)	TWR (mm)	ROC (mm)
1	2	1.5	6.0	168.94	0.024	0.022
2	2	2.5	5.5	181.45	0.025	0.027
3	2	3.5	5.0	195.5	0.026	0.029
4	4	1.5	5.5	181.43	0.024	0.027
5	4	2.5	5.0	188.39	0.026	0.030
6	4	3.5	6.0	204.08	0.027	0.033
7	6	1.5	5.0	188.38	0.025	0.029
8	6	2.5	6.0	195.91	0.027	0.033
9	6	3.5	5.5	204.06	0.029	0.038

3. Results and discussion

The regression equation was developed using MINITAB to evaluate the predicted value of outputs. The influence of input parameters on MRR, TWR and ROC for Al-SiC of various compositions are analysed using ANOVA as shown in Tables 6-8.

3.1 Metal Removal Rate (MRR)

Main effect plots for MRR for three different compositions of SiC is plotted against pulse on (C1), peak current (C2) and electrode gap (C3), is explained in Figs. 2, 3 & 4.

Table 5. Taguchi L_9 experimental runs for Al-SiC 9%.

Trial no.	Pulse on (µs)	Peak current (A)	Electrode gap (mm)	MRR (mm³/min)	TWR (mm)	ROC (mm)
1	2	1.5	6.0	129.91	0.027	0.023
2	2	2.5	5.5	140.72	0.030	0.026
3	2	3.5	5.0	158.30	0.031	0.029
4	4	1.5	5.5	144.72	0.029	0.027
5	4	2.5	5.0	158.28	0.032	0.031
6	4	3.5	6.0	174.65	0.035	0.034
7	6	1.5	5.0	163.37	0.032	0.028
8	6	2.5	6.0	168.80	0.036	0.032
9	6	3.5	5.5	187.55	0.039	0.037

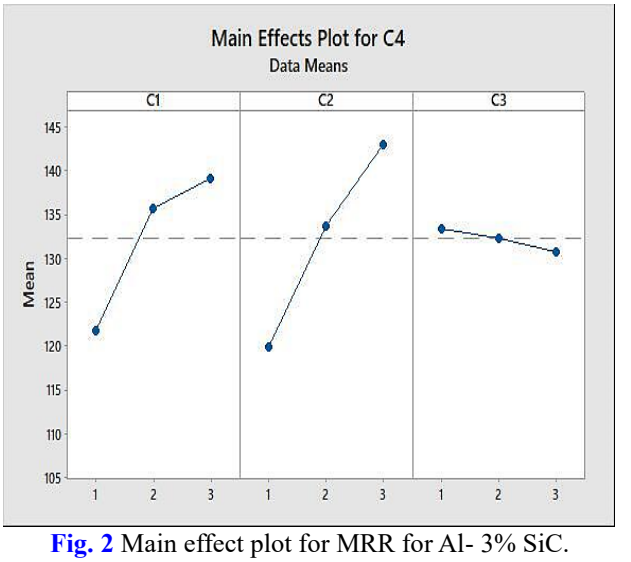

Fig. 2 Main effect plot for MRR for Al- 3% SiC.

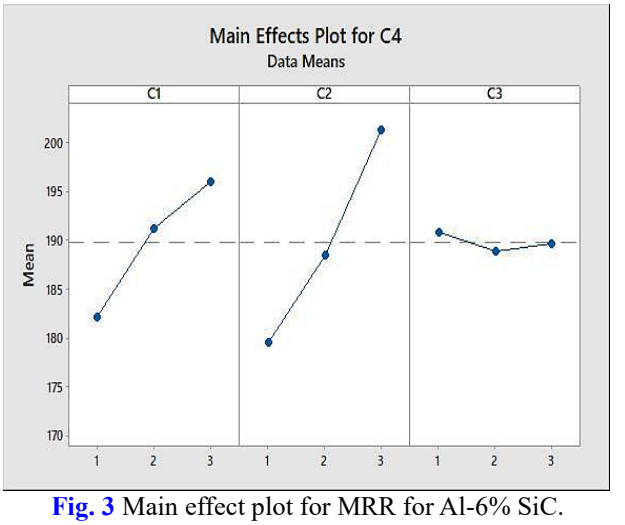

Fig. 3 Main effect plot for MRR for Al-6% SiC.

MRR was found to be higher for larger current and pulse ON-time settings at the expense of tapercity, radial overcut and surface finish.[5]

3.2 Tool Wear Ratio (TWR)

Main effect plots for TWR for three different compositions of SiC is plotted against pulse on (C1), peak current (C2) and

electrode gap (C3), is explained in Figs. 5, 6 & 7. TWR was also found to be higher, for larger current settings. Electrode gap has considerable effect on the MRR and TWR.[5]

3.3 Radial Over Cut (ROC)

Main effect plots for ROC for three different compositions of SiC is plotted against pulse on (C1), peak current (C2) and electrode gap (C3), is explained in Figs. 8, 9 & 10. The MRR and ROC increases with increase in non-linear fashion with increase in peak current and pulse duration.[16]

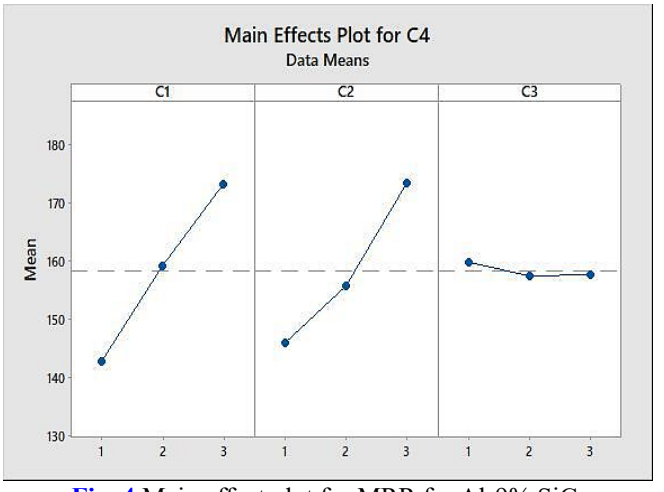

Fig. 4 Main effect plot for MRR for Al-9% SiC.

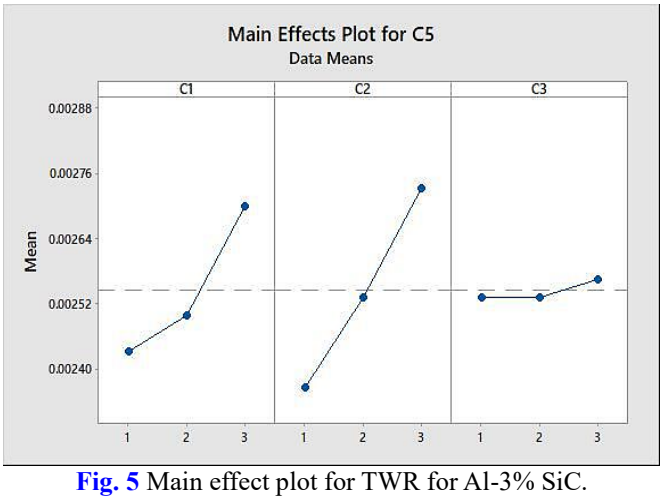

Fig. 5 Main effect plot for TWR for Al-3% SiC.

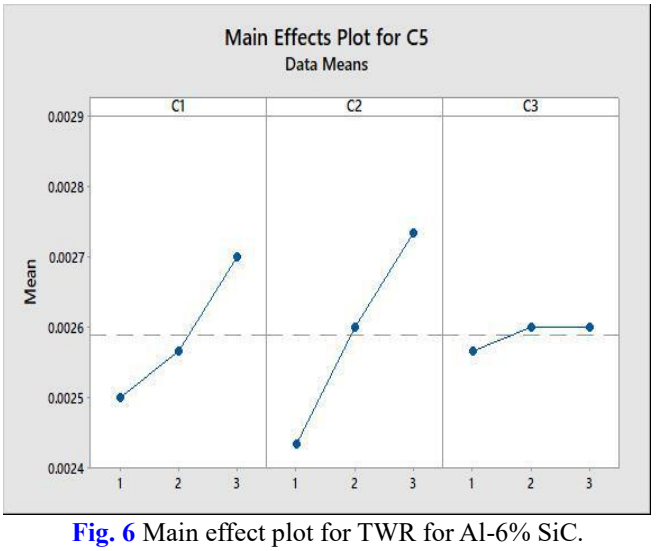

Fig. 6 Main effect plot for TWR for Al-6% SiC.

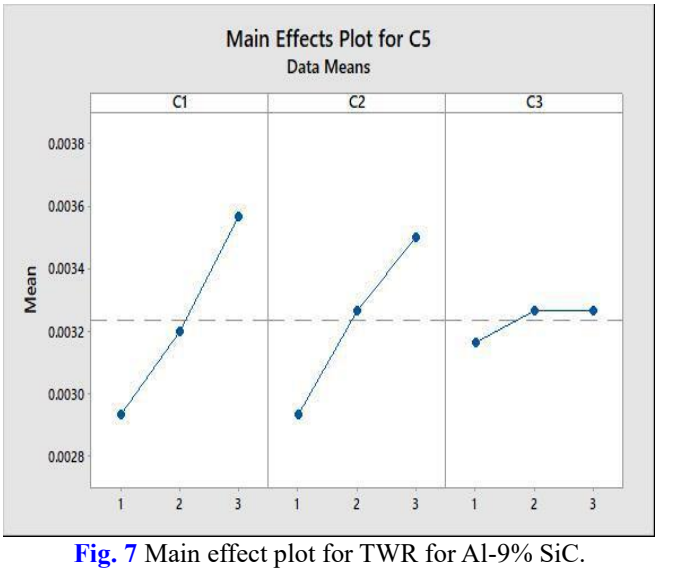

Fig. 7 Main effect plot for TWR for Al-9% SiC.

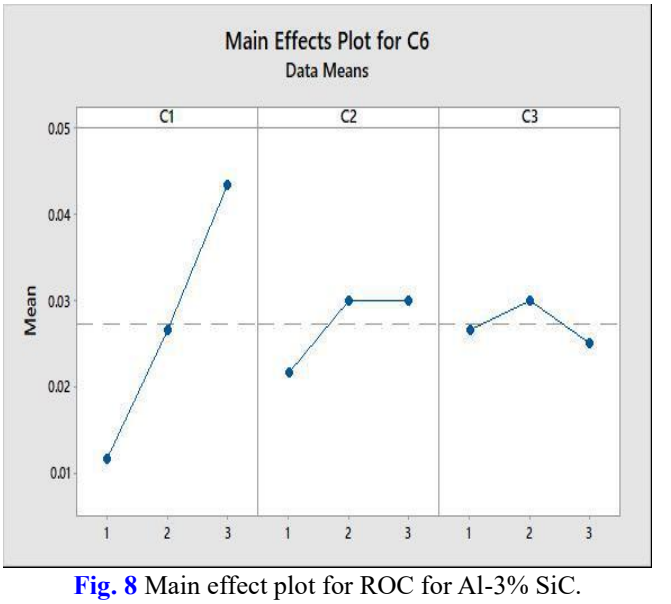

Fig. 8 Main effect plot for ROC for Al-3% SiC.

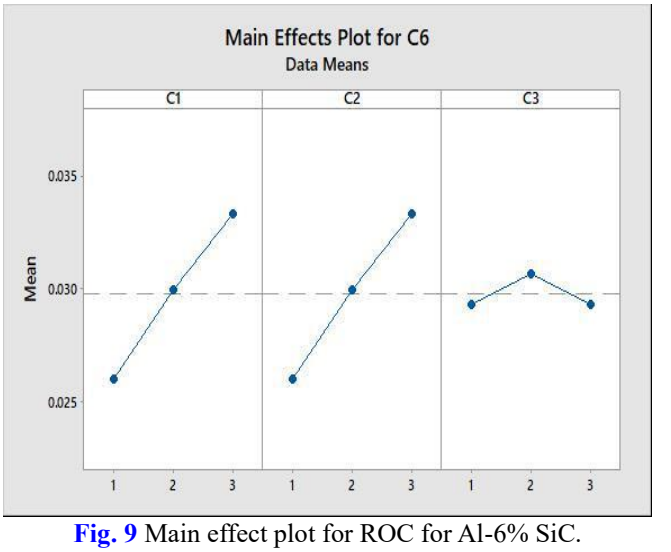

Fig. 9 Main effect plot for ROC for Al-6% SiC.

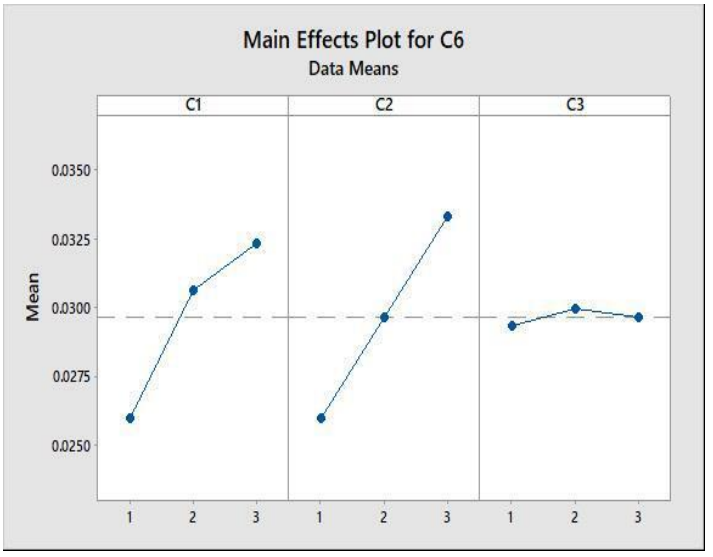

Fig. 10 Main effect plot for ROC for Al-9% SiC.

3.4 Influence of input parameters

The influence of input parameters on MRR, TWR and ROC for Al-3% SiC is shown in Tables 6-8.

Table 6. Influence of process parameters on MRR for Al-3% SiC.

Levels	P1(Pulse On)	P2(Peak Current)	P3(Electrode Gap)
L1	121.76	120.01	133.45
L2	135.76	133.72	132.42
L3	139.22	143.01	130.87
DELTA	17.46	23	2.58
RANK	2	1	3

Table 7. Influence of process parameters on TWR for Al-3% SiC.

Levels	P1(Pulse On)	P2(Peak Current)	P3(Electrode Gap)
L1	0.024	0.024	0.025
L2	0.025	0.025	0.025
L3	0.027	0.029	0.027
DELTA	0004	0.005	0.002
RANK	2	1	3

Table 8. Influence of process parameters on ROC for Al-3% SiC.

Levels	P1(Pulse On)	P2(Peak Current)	P3(Electrode Gap)
L1	0.011	0.026	0.021
L2	0.026	0.090	0.030
L3	0.043	0.075	0.030
DELTA	0.032	0.064	0.009
RANK	2	1	3

Tables 6-8 show the influence of input parameters on all three response parameters of Al-3% SiC. The peak current and the pulse on time have a major impact on the response parameters. The electrode gap has very little influence on the response parameters.

Tables 9-11 show the influence of input parameters on all three response parameters of Al-6% SiC.

Table 9. Influence of process parameters on MRR for Al-6% SiC.

Levels	P1(Pulse On)	P2(Peak Current)	P3(Electrode Gap)
L1	182.1	179.58	190.90
L2	191.3	188.58	188.98
L3	196.11	201.36	189.64
DELTA	14.01	21.78	1.26
RANK	2	1	3

Table 10. Influence of process parameters on TWR for Al-6% SiC.

Levels	P1(Pulse On)	P2(Peak Current)	P3(Electrode Gap)
L1	0.025	0.025	0.025
L2	0.025	0.026	0.026
L3	0.027	0.027	0.026
DELTA	0.002	0.003	0.001
RANK	2	1	3

Table 11. Influence of process parameters on ROC for Al-6% SiC.

Levels	P1(Pulse On)	P2(Peak Current)	P3(Electrode Gap)
L1	0.026	0.026	0.029
L2	0.030	0.129	0.027
L3	0.033	0.033	0.029
DELTA	0.007	0.103	0.002
RANK	2	1	3

The increase in current the spark energy increases which melts and evaporates the material from the workpiece. The above table shows the influence of input parameters on all three response parameters of Al-6% SiC. The peak current and the pulse on time have a major impact on the response parameters. The electrode gap has very little influence on the response parameters.

The peak current and the pulse on time have a major impact on the response parameters. The increase in current the spark energy increases which melts and evaporates the material from the workpiece. Figs. 2-10 shows the variation of MRR with Pulse on Time and it was observed that with an increase in Pulse on Time, MRR decreases. Figs. 11 and 12 show the variation of MRR with Gap Voltage and it was observed that at first MRR increases with an increase in Gap Voltage and after reaching a certain value it starts decreasing. An increase in voltage increases current which removes material from the workpiece. The electrode gap has very little influence on the response parameters.

The influence of input parameters on MRR, TWR and ROC for Al-9% SiC are tabulated below in Tables 12-14.

3.5 Analysis of Variance (ANOVA)

Analysis of variance for MRR, TWR and ROC was analysed for Al-3% SiC, Al-6% SiC composition and Al-9% SiC composition and displayed in Tables 15-23.

Analysis of variance for material removal rate (MRR), tool wear ratio (TWR) and radial over cut (ROC) was analysed for Al-3% SiC composition.

Analysis of variance for material removal rate (MRR), tool wear ratio (TWR) and radial over cut (ROC) was analysed for Al-6% SiC composition.

Table 12. Influence of process parameters on MRR for Al-9% SiC.

Levels	P1(Pulse On)	P2(Peak Current)	P3(Electrode Gap)
L1	146	142.97	159.98
L2	155.93	159.21	157.66
L3	173.50	173.24	157.78
DELTA	27.5	30.27	2.2
RANK	2	1	3

Table 13. Influence of process parameters on TWR for Al-9% SiC.

Levels	P1(Pulse On)	P2(Peak Current)	P3(Electrode Gap)
L1	0.029	0.029	0.031
L2	0.032	0.032	0.032
L3	0.035	0.036	0.032
DELTA	0.006	0.007	0.001
RANK	2	1	3

Table 14. Influence of process parameters on ROC for Al-9% SiC.

Levels	P1(Pulse On)	P2(Peak Current)	P3(Electrode Gap)
L1	0.026	0.026	0.029
L2	0.029	0.030	0.027
L3	0.030	0.032	0.029
DELTA	0.004	0.006	0.002
RANK	2	1	3

Table 15. ANOVA for MRR.

Source	DF	Adj SS	Adj MS	F-Value	P-Value	% contribution
Regression	3	0.001613	0.000538	28.88	0.001	91.76
C1	1	0.001504	0.001504	80.82	0.000	33.30
C2	1	0.000104	0.000104	5.60	0.064	57.73
C3	1	0.000004	0.000004	0.22	0.656	0.73
Error	5	0.000093	0.000019			8.24
Total	8	0.001706				

Table 16. ANOVA for TWR.

Source	DF	Adj SS	Adj MS	F-Value	P-Value	% contribution
Regression	3	0.000031	0.000010	42.27	0.001	96.21
C1	1	0.000011	0.000011	43.64	0.001	34.37
C2	1	0.000020	0.000020	82.50	0.000	62.50
C3	1	0.000000	0.000000	0.68	0.447	0.01
Error	5	0.000001	0.000000			3.12
Total	8	0.000032				

Table 17. ANOVA for ROC.

Source	DF	Adj SS	Adj MS	F-Value	P-Value	% contribution
Regression	3	1260.45	420.150	18.55	0.004	94.54
C1	1	457.45	457.452	20.20	0.006	41.09
C2	1	793.04	793.040	35.02	0.002	54.15
C3	1	9.96	9.959	0.44	0.537	2.31
Error	5	113.24	22.647			5.45
Total	8	1373.69				

Table 18. ANOVA for MRR.

Source	DF	Adj SS	Adj MS	F-Value	P-Value	% contribution
Regression	3	0.000161	0.000054	63.68	0.000	94.99
C1	1	0.000081	0.000081	95.53	0.000	27.70
C2	1	0.000081	0.000081	95.53	0.000	67.05
C3	1	0.000000	0.000000	0.00	1.000	0.24
Error	5	0.000004	0.000001			5.01
Total	8	0.000166				

Table 19. ANOVA for TWR.

Source	DF	Adj SS	Adj MS	F-Value	P-Value	% contribution
Regression	3	0.000020	0.000007	26.82	0.002	94.15
C1	1	0.000006	0.000006	24.55	0.004	28.57
C2	1	0.000013	0.000013	55.23	0.001	61.90
C3	1	0.000000	0.000000	0.68	0.447	4.77
Error	5	0.000001	0.000000			4.76
Total	8	0.000021				

Table 20. ANOVA for ROC.

Source	DF	Adj SS	Adj MS	F-Value	P-Value	% contribution
Regression	3	1007.88	335.959	31.58	0.001	97.45
C1	1	293.93	293.930	27.63	0.003	47.79
C2	1	711.55	711.553	66.88	0.000	48.79
C3	1	2.39	2.394	0.23	0.655	0.02
Error	5	53.20	10.640			2.40
Total	8	1061.08				

Table 21. ANOVA for MRR.

Source	DF	Adj SS	Adj MS	F-Value	P-Value	% contribution
Regression	3	2515.42	838.47	98.40	0.000	98.33
C1	1	1373.80	1373.80	161.23	0.000	44.87
C2	1	1134.38	1134.38	133.13	0.000	57.35
C3	1	7.24	7.24	0.85	0.399	0.11
Error	5	42.60	8.52			1.67
Total	8	2558.02				

Table 22. ANOVA for TWR.

Source	DF	Adj SS	Adj MS	F-Value	P-Value	% contribution
Regression	3	0.000110	0.000037	84.49	0.000	98.07
C1	1	0.000060	0.000060	138.85	0.000	42.57
C2	1	0.000048	0.000048	111.15	0.000	53.85
C3	1	0.000002	0.000002	3.46	0.122	1.80
Error	5	0.000002	0.000000			1.78
Total	8	0.000112				

Table 23. ANOVA for ROC.

Source	DF	Adj SS	Adj MS	F-Value	P-Value	% contribution
Regression	3	0.000141	0.000047	33.57	0.001	95.27
C1	1	0.000060	0.000060	42.98	0.001	40.54
C2	1	0.000081	0.000081	57.62	0.001	54.72
C3	1	0.000000	0.000000	0.12	0.744	0.02
Error	5	0.000007	0.000001			4.72
Total	8	0.000148				

Analysis of variance for material removal rate (MRR), tool wear ratio (TWR) and radial over cut (ROC) was analysed for Al-9% SiC composition.

3.6 Comparison of Conventional and Un-Conventional machining

To study the material well an experiment was conducted using conventional machining for the same material, Aluminium Silicon Carbide of various compositions 3%, 6% and 9% was considered. Nickel nickel-coated tool was used for this process. The process was done taking feed and speed into consideration. The tool material was kept constant, feed was varied 0.7, 0.8 & 0.9 mm/rev and speed was varied to 750, 800 & 850 rpm. The major idea behind this drilling process is to compare the results between the non-conventional and conventional drilling process on Aluminium Silicon Carbide material and the results were obtained as shown in Tables 24-26.

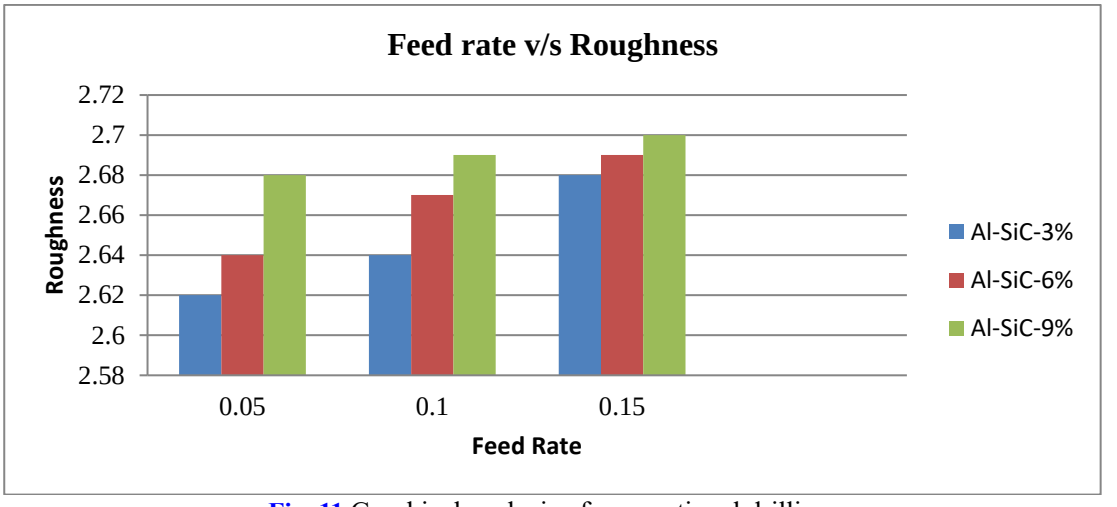

Fig. 11 Graphical analysis of conventional drilling.

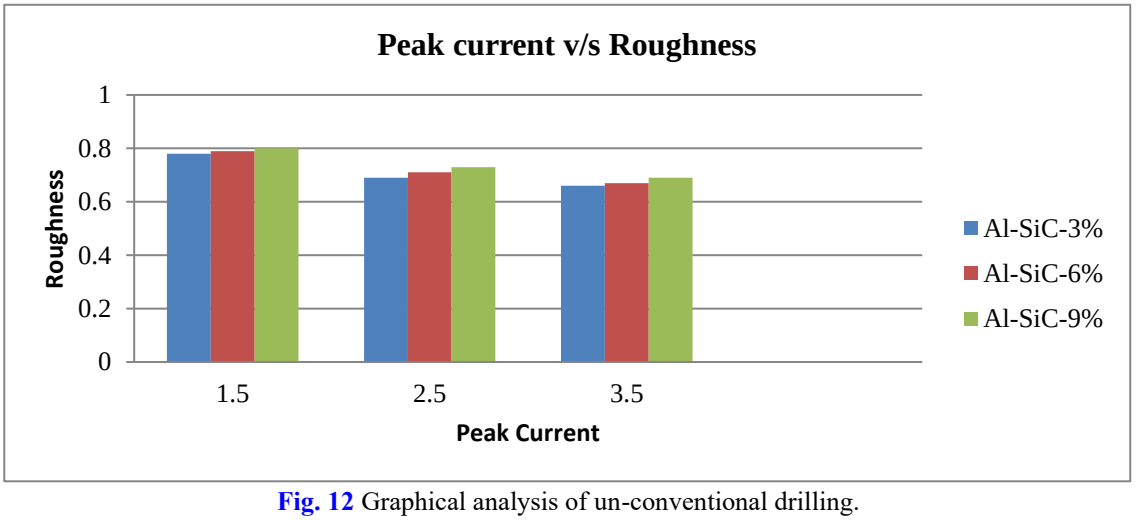

Fig. 12 Graphical analysis of un-conventional drilling.

Table 24. Roughness values for conventional and un-conventional drilling Al-3%SiC.

Trial	Roughness for un-conventional drilling	Roughness for conventional drilling
	Al-Sic-3%	Al-Sic-3%
1	0.71	2.74
2	0.86	295
3	0.79	2.72
4	0.70	2.69
5	0.53	2.51
6	0.84	2.82
7	0.58	2.55
8	0.66	2.69
9	0.74	2.80

Table 25. Roughness values for conventional and un-conventional drilling Al-6%SiC.

Trial	Roughness for un-conventional drilling	Roughness for conventional drilling
	Al-Sic-6%	Al-Sic-6%
1	0.74	2.79
2	0.88	2.92
3	0.75	2.75
4	0.72	2.79
5	0.55	2.64
6	0.86	2.59
7	0.54	2.77
8	0.62	2.56
9	0.73	2.71

3.6.1 Conventional drilling

It is evident from the graph that surface roughness increases with increase in feed rate. As the percentage of silicon carbide increases, roughness also increases with increase in feed rate.

3.6.2 Un-Conventional

It is evident from the graph that surface roughness increases with increase in peak current. As the percentage of silicon carbide increases, roughness decreases with increase in peak current.

Table 26. Roughness values for conventional and un-conventional drilling Al-9%SiC.

Trial	Roughness for un-conventional drilling	Roughness for conventional drilling
	Al-Sic-9%	Al-Sic-9%
1	0.72	2.79
2	0.87	2.94
3	0.76	2.77
4	0.71	2.81
5	0.57	2.69
6	0.89	2.64
7	0.53	2.77
8	0.65	2.58
9	0.76	2.75

3.6.3 Confirmation Experiments

After getting the optimum set of input parameters through Taguchi orthogonal array and ANOVA, again machining was carried out with the same set of input parameters and MRR, TWR and Radial Overcut were again calculated which was found to be approximately same as the previous values.

4. Conclusion

The machinability of Aluminium Silicon Carbide composites using conventional machining methods and comparing the results with the un-conventional machining method (EDM) were performed. This research also evaluates the feasibility of electric discharge machining of Al-3% SiC, Al-6% SiC and Al-9% SiC composites. The MRR, TWR and ROC increases significantly in a non- linear fashion with increase in current. The material removal rate and radial over cut increases with increase in the intensity of the pulse. The electrode gap was found to have a very little effect on the three responses. It is evident that the MRR of the Aluminium composites is more in un-conventional method than in conventional method because of the influence of the effect of the high intensity of the peak current. The surface roughness is more in conventional method than in un-conventional method. The flushing pressure of the dielectric fluid and proper setting of the pulse on time in un-conventional method helps in providing a better finish than the conventional machining method. It is evident that un-conventional machining method is more feasible that the conventional method for machining Aluminium Silicon Carbide composites.

Conflict of Interest

There is no conflict of interest.

Supporting Information

Not applicable.

References

[1] K. Jain, V. Agarwal, S. S. Ahmad, S. Mohapatra, P. K. Srivastava, P. B M, R. Bhat, Multi-parametric Optimization of Wired Electrical Discharge Machining Process to Minimize Damage Cause in Steel - A soft computing-based Taguchi-Grey Relation Analysis Approach, *Engineered Science*, 2022, **20**, 267-274, doi: 10.30919/es8e729.

[2] K. J. Santosh Kumar, G. A. Bhargav, Y. Naik, K. Bommanna, Friction stir welding of different aluminum-silicon alloy compositions utilizing conventional vertical milling machine, *Journal of Computers, Mechanical and Management*, 2022, **1**, 28-37, doi: 10.57159/gadl.jcmm.1.1.22012.

[3] G. B. Kamath, K. Subramaniam, S. Devesh, V. Chavan, N. Mohan, R. Bhat, H. T. Wijerathne, Multi-response optimization of milling process parameters for aluminium-titanium diboride metal matrix composite machining using taguchi- data envelopment analysis ranking approach, *Engineered Science*, 2022, **18**, 271-277, doi: 10.30919/es8d680.

[4] N. P. Hung, L. J. Yang, K. W. Leong, Electrical discharge machining of cast metal matrix composites, *Journal of Materials Processing Technology*, 1994, **44**, 229-236, doi: 10.1016/0924-0136(94)90435-9.

[5] K. H. Ho, S. T. Newman, State of the art electrical discharge machining (EDM), *International Journal of Machine Tools and Manufacture*, 2003, **43**, 1287-1300, doi: 10.1016/S0890-6955(03)00162-7.

[6] A.L. Livshits, Introduction, in: Electro-erosion Machining of Metals, Department of Scientific& Industrial Research, Butterworth & Co., London, 1960, doi: 10.1149/1.2427956.

[7] B. Nahak, A. Gupta, A review on optimization of machining performances and recent developments in electro discharge machining, *Manufacturing Review*, 2019, **6**, 2, doi: 10.1051/mfreview/2018015.

[8] E.C. Jameson, Description and development of electrical discharge machining (EDM), in: Electrical Discharge Machining, Society of Manufacturing Engineers, Dearbern, Michigan, 2001.

[9] Y.-P. Zeng, C.-L. Lin, H.-M. Dai, Y.-C. Lin, J.-C. Hung, Multi-performance optimization in electrical discharge machining of Al_2O_3 ceramics using taguchi base AHP weighted TOPSIS method, *Processes*, 2021, **9**, 1647, doi: 10.3390/pr9091647.

[10] P. N. Singh, K. Raghukandan, M. Rathinasabapathi, B. C. Pai, Electric discharge machining of Al–10%SiC_P as-cast metal matrix composites, *Journal of Materials Processing Technology*, 2004, **155-156**, 1653-1657, doi: 10.1016/j.jmatprotec.2004.04.321.

[11] P. N. Singh, K. Raghukandan, B. C. Pai, Optimization by Grey relational analysis of EDM parameters on machining Al–10%SiC_P composites, *Journal of Materials Processing Technology*, 2004, **155-156**, 1658-1661, doi: 10.1016/j.jmatprotec.2004.04.322.

[12] H.-P. Nguyen, V.-D. Pham, N.-V. Ngo, Application of TOPSIS to Taguchi method for multi-characteristic optimization of electrical discharge machining with titanium

powder mixed into dielectric fluid, *The International Journal of Advanced Manufacturing Technology*, 2018, **98**, 1179-1198, doi: 10.1007/s00170-018-2321-2.
[13] B. Mohan, A. Rajadurai, K. G. Satyanarayana, Electric discharge machining of Al–SiC metal matrix composites using rotary tube electrode, *Journal of Materials Processing Technology*, 2004, **153-154**, 978-985, doi: 10.1016/j.jmatprotec.2004.04.347.
[14] C. C. Wang, B. H. Yan, Blind-hole drilling of Al_2O_3/6061Al composite using rotary electro-discharge machining, *Journal of Materials Processing Technology*, 2000, **102**, 90-102, doi: 10.1016/S0924-0136(99)00423-9.
[15] A. Yadav, Y. Singh, S. Singh, P. Negi, Sustainability of vegetable oil based bio-diesel as dielectric fluid during EDM process–A review, *Materials Today: Proceedings*, 2021, **46**, 11155-11158, doi: 10.1016/j.matpr.2021.01.967.
[16] K. H. Syed, G. P. Anuraag, G. Hemanth, S. A. Subahan, Powder-mixed EDM machining of aluminium-silicon carbide composites, *Indian Journal of Science and Technology*, 2015, **8**, 133, doi: 10.17485/ijst/2015/v8is2/59170.
[17] B.-H. Yan, C.-C. Wang, Machinability of SiC particle reinforced aluminum alloy composite material, *Journal of Japan Institute of Light Metals*, 1993, **43**, 187-192, doi: 10.2464/jilm.43.187.
[18] V. Srikanth, S. Kowshik, D. Narasimha, S. Patil, K. Samanth, U. Rathee, Finite element modelling and analysis of fiber reinforced concrete under tensile and flexural loading, *Journal of Computers, Mechanical and Management*, 2022, **1**, 11-17, doi: 10.57159/gadl.jcmm.1.1.22004.
[19] J. Monaghan, P. O'Reilly, The drilling of an Al/SiC metal-matrix composite, *Journal of Materials Processing Technology*, 1992, **33**, 469-480, doi: 10.1016/0924-0136(92)90280-6.
[20] L. A. Looney, J. M. Monaghan, P. O'Reilly, D. M. R. Taplin, The turning of an Al/SiC metal-matrix composite, *Journal of Materials Processing Technology*, 1992, **33**, 453-468, doi: 10.1016/0924-0136(92)90279-2.
[21] M. Kathiresan, T. Sornakumar, EDM studies on aluminum alloy-silicon carbide composites developed by vortex technique and pressure die casting, *Journal of Minerals and Materials Characterization and Engineering*, 2010, **9**, 79-88, doi: 10.4236/jmmce.2010.91007.
[22] J. D. Marafona, A. Araújo, Influence of workpiece hardness on EDM performance, *International Journal of Machine Tools and Manufacture*, 2009, **49**, 744-748, doi: 10.1016/j.ijmachtools.2009.03.002.
[23] R. Karthikeyan, P. R. Lakshmi Narayanan, R. S. Naagarazan, Mathematical modelling for electric discharge machining of aluminium–silicon carbide particulate composites, *Journal of Materials Processing Technology*, 1999, **87**, 59-63, doi: 10.1016/S0924-0136(98)00332-X.
[24] S. Dhar, R. purohit, N. Saini, A. Sharma, G. Hemanth Kumar, Mathematical modelling of electric discharge machining of cast Al-4Cu-6Si alloy-10wt.% SiC composites, *Journal of Materials Processing Technology*, 2007, **194**, 24-29, doi: https://doi.org/10.1016/j.jmatprotec.2007.03.121.
[25] M. P. Jenarthanan, S. Ramesh, Optimization of process conditions of Powder Mixed Electric Discharge Machining of Nickel based Superalloy using Grey Wolf Optimizer algorithm, Proceedings of the Institution of Mechanical Engineers, Part C: Journal of Mechanical Engineering Science, 2023, doi: 10.1177/09544062231187789.

BENTHAM SCIENCE

CrossMark

Current Medical Imaging

Content list available at: https://benthamscience.com/journals/cmir

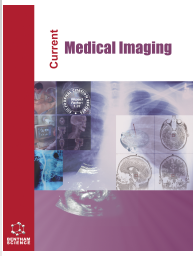

RESEARCH ARTICLE

Modified Exigent Features Block in JAN Net for Analysing SPECT Scan Images to Diagnose Early-Stage Parkinson's Disease

Jothi Siluvaimuthu[1], Anita Sebasthiyar[2] and Sivakumar Subburam[3,*]

[1]*Department of Computer Science, Jayaraj Annapackiam College for Women, M. K. University, Madurai, Tamilnadu, India*
[2]*Department of Electronics and Communication Engineering, St. Anne's College of Engineering and Technology, Anna University, Chennai, Tamilnadu, India*
[3]*Department of Computer Science, Cardamom Planters' Association College, M. K. University, Madurai, Tamilnadu, India*

Abstract:

Background:

The quantitative measure of dopamine transporter (DaT) in the human midbrain is generally used as a biomarker for analyzing Parkinson's disease (PD).

Introduction:

DaT scan images or Single- photon emission computed tomography (SPECT) images are utilized to capture the dopamine content more accurately.

Methods:

Only sixteen slices out of ninety-one of SPECT images were chosen on the basis of the high amount of dopamine content and were named Volume rendering image slices (VRIS). This paper proposes a novel Convolutional Neural Network (CNN) called JAN Net which particularly treats the VRIS for identifying PD. The JAN Net preserves the edges and spatial features of the striatum by using a modified exigent feature (M-ExFeat) block, that contains convolutional and additive layer. The different-sized convolutional layer extracts both low- and high-level features of Striatum. The additive layer adds up all the features of different filter sized convolutional layers like 1x1, 3x3, and 5x5. The added output features are used to improve the learnability of neurons in the hidden layer. The network performance is tested for stride 1 and stride 2.

Results:

The results are validated using the dataset taken from the Parkinson's Progression Markers Initiative (PPMI) database. The JAN Net ensures improved performance in terms of accuracy. The training and validation accuracy for stride 2 is 100% with minimum losses. The outcome has been compared with different deep learning architectures and the machine learning techniques like Extreme Learning Machines (ELM), and Artificial Neural Networks (ANN) to highlight the efficacy of the proposed architecture.

Conclusion:

Hence, the present work could be of great aid to the experts in neurology to protect the neurons from impairment.

Keywords: Early PD, CNN, Modified exfeat, Performance, JAN network, Artificial intelligence.

Article History	Received: July 29, 2022	Revised: November 27, 2022	Accepted: December 29, 2022

1. INTRODUCTION

Parkinson's disease (PD) is the most common neurode generative or movement disorder, caused due to deterioration of dopaminergic neurons in the human brain in the region of Substantia Nigra (SN). Owing to it, patients' behavioral, cognitive, and functional systems get progressively spoiled, and such non-motor and motor issues are observable corresponding to the reducing number of dopaminergic neurons [1 - 3]. Statistically, around ten million people have become victims of PD [4, 5] worldwide. As these symptoms of

* Address correspondence to this author at the Department of Computer Science, Cardamom Planters' Association College, M. K. University, Madurai, Tamilnadu, India; Tel: +91 6380757396; E-mail: sivakumar_s@cpacollege.org

the disorder are common to every neurological disease, the danger of mistaking PD for some other neurological disease or vice versa is extensively possible.

Affirming the possibility, it is detected that about twenty-five percent of the identification is misdiagnosed. Hence, evolving a method for the precise identification of PD is very imperative.

Imaging modalities like single-photon emission computerized tomography (SPECT), magnetic resonance imaging (MRI), positron emission tomography (PET), and functional MRI (fMRI) are used to perceive the degradation of neurons caused by the continual biochemical (dopaminergic neurons) change in the striatum and thus PD is identified. Among them, SPECT images offer the accurate identification of dopamine content at an early stage and minimize interobserver variability [6]. Parkinson's Progression Markers Initiative (PPMI), a longitudinal database avail such dopamine transporter (DaT) images and those are picked up to show forth dopamine content in diagnosing the disease. A number of research on the SPECT images are steadily growing in treating the disease in an advanced manner [7].

Diagnosing process of Early Parkinson's disease (EPD) using SPECT images was done through the visual appearance of the striatum. Although it required a great amount of time, the differences in the findings of experts confirmed the results are unreliable. Moreover, in the case of feature extraction from 2D slices [7] and then averaged image slice of SPECT image [8], the changes in DaT content and the shape of the striatum during the premature stage could be monitored through the implementation of the analysis of 3D slices [9]. Yet, clinical practitioners seldom wish to utilize it on account of the complexity of the analysis of 3D slices. Hence, it was a felt need for a simpler technique to identify EPD assuring a better result in terms of accuracy. In this regard, Anita *et al*. [10] proposed a model taking only 12 slices from a SPECT image for the analysis. It fell short of diagnosing EPD accurately as the shape of the striatum could not be comprehended well, since a few more slices were also responsible for the complete comprehension of the shape of the striatum. Accordingly, slices from 34 to 49 were taken into analysis which helped to have a complete comprehension of the shape which assureed the accurate diagnosis of EPD. Thus, a novel method is proposed using those 16 slices as a two-dimensional slice to improve diagnostic accuracy.

Normally, PD patients are classified with the help of Machine Learning (ML) algorithms such as Support Vector Machine (SVM), Extreme Learning Machine (ELM), and Artificial Neural Networks (ANN). However, the output result received from them lacked precision due to their manipulation of the data. Owing to it, of late these algorithms are replaced by different deep neural networks (DNN) and it is a revolution in the diagnosing process as it helps to study even complicated features involved in detecting PD in its initial stage. Precise image classification and segmentation are made possible by the application of different deep convolutional neural networks (CNN) [11 - 13] and some of them are AlexNet [12], VGG-Net [14], ResNet [15], and GoogleNet [16]. AlexNet [12] introduces the very concept of dropout and data augmentation respectively to lower the problem of overfitting and to enhance the impressive preciseness of the network. Also, VGG-Net [14] has accomplished good efficiency for the image Net dataset. VGG-Net is combined with residual module and frames ResNet [15]. The residual module brings the response of the processed layer along with the response of the previous layer to improve the capability of studying the edge features more accurately. These edge features are given to the ResNet to increase the effectiveness of the network. Another network named GoogleNet [16], designed by Szegedy *et al*. incorporates 22 CNN layers with the inception module.

Ortiz *et al*. [17] designed an architecture, using LeNet 5 and AlexNet, which is capable of classifying the cases of Parkinson's disease from Healthy Normal (HN) based on DaT scan images taken from the PPMI database [18]. This network offers good discriminative ability in terms of accuracy, sensitivity, specificity, and Area Under Curve (AUC). Another CNN module proposed by Martin *et al*. [19] is highly trained to discriminate drawing movements of PD patients from HN. The network includes two parts, of which one is for feature selection and the other for classification. The performance of the network has been evaluated using accuracy, F1-score, and an AUC. Monu Verma *et al*. designed an Exigent Feature Preservative Network (EXPERTNet) to recognize facial expressions. The Exigent Feature layer (ExFeat) and additive module in the network function to preserve both micro and macro features. Moreover, the convolutional layer with different- sized filters allows the discriminator to reach a decision more effectively [20]. Though the performance is more effective, the EXPERT network is quite complex for analyzing SPECT images.

Motivated by all the earlier works in the literature, a new, simple, and accurate architecture, named JAN Net, is evolved to preserve all essential features in the process of identifying EPD. The key features of JAN Net are briefed as:

1. A novel methodology is found to detect early Parkinson's Disease using SPECT images. Each SPECT image has 91 slices. Out of these, only 16 slices, that is slices from 34 to 49, show a high striatal uptake region. Hence, those 16 slices are chosen for the purpose of diagnostic accuracy [10]. Further, changes in the shape of the striatum are also analyzed completely from those slices.

2. The shape of the striatum is the key biomarker for identifying PD. This could be understood by the edge and position of the pixel which is extracted by the filters used in the modified EX-FEAT block. The size of the filter used in this block is 1x1, 3x3, and 5x5, and the depth is 32 which help to make an accurate decision on the shape of the striatum. The additive block is designed to add the key features of all convolutional layers parallelly and serially to facilitate effective discrimination between early PD and HN.

3. The new JAN network, constituted of a modified ExFeat block is designed to identify EPD. The different-sized filters of the modified ExFeat block extract the relevant features (micro and macro level edge features) to reduce the hyper-parameters of the hidden layers that minimize the computational complexity and enhance the accurate performance.

2. COMPUTATIONAL METHODS

2.1. Study Cohort in Detail

Diagnosing EPD is quite a challenging task as it has symptoms similar to other neuro-disorders and PD in its early stage cannot be diagnosed with the help of such symptoms. A novel network called JAN Net, therefore, has been designed to diagnose EPD using SPECT images. The input images for the network are chosen from the PPMI database which collects the images of PD patients and HN internationally as it is the first large, multi-center database to comprehend PD and to understand the etiology of the disease as well. It is also collaborated with partners around the world to identify the multiple dimensions of the disease. The SPECT images in the database are categorized as EPD and HN by the experts. Among the 620 images collected for our purpose, 190 images were of HN, and the rest 430 images of EPD patients. The EPD patients are taken on the basis of Hohen and Yahr stage (H&Y) 1 and 2 criteria with the mean as 1.50± 0. 50. All the images taken from the database are pre-processed images. The preprocessing steps are as follows: The raw SPECT images are iteratively reconstructed to maintain the reliability of the process. Then, the attenuation correction and spatial normalization are done to normalize and confirm the same anatomical alignment of the images [20] throughout the database. The final processed image has dimensions 91x109x91 cubic with a 2mm width in DICOM format.

2.2. Selection of High Striatal Uptake Image Slices

The SPECT images were captured as the drug-gets-bound with the DaT content found in the brain. These captured images have different shapes of the striatum in two different subjects. Image slices that are beneficial to differentiate EPD and HN were chosen for our study. Total ninety-one slices were found in a captured SPECT image [8] which is observed from the bottom and running to the top of the brain. Slices that indicate high specific uptake were selected from 91 slices as a novel diagnostic tool. In order to make this analysis as simple as possible, the remaining slices were not included in our investigation as the striatal uptake region gets steadily condensed (to the level that uptake could hardly be noticed). This leads to getting greater accuracy in identifying the disease as per the direction laid by the Society of Nuclear Medicine (SNM) [21].

Prashanth *et al*. [8] following the direction of SNM worked out the mean area of slices from 34 to 49 which have high striatal uptake region. Anita *et al*. selected only 12 slices to find an accurate system for diagnosing EPD, but the choice of 16 slices and the analysis renders greatly improved performance. The individual 16 slices are combined as a two-dimensional slice to make the analysis as depicted in (Fig. **1**). These selected 16 image slices render volume information from the 2D image slices. Hence, it is called volume rendering image slices. Moreover, it is a simpler technique that assures a better performance than the 12 VRIS [10, 11] as EPD directly affects the size of the striatum. Therefore, VRIS is selected as it provides the continuity of the shape of the striatum.

3. PROPOSED ARCHITECTURAL DESIGN

The selected VRIS of early PD and HN are given in (Fig. **2**). The image claims that the ‘dot-shaped striatum denotes EPD and ‘comma-shaped striatum denotes HN. These images are processed by a novel neural network architecture for diagnosing early PD and it is named JAN Net. The three significant layers of the proposed JAN architecture are convolutional layers, Modified Exigent Feature (M-ExFeat) block, and fully connected layer (FCL) as shown in (Fig. **3**). The JAN Net is started with convolutional layers [each includes the convolutional layer and the activation layer called Rectified linear unit (ReLu)] that has a depth of 32 and size of 5×5 and 3×3 filters. The input for the JAN network is volume rendering image slices (VRIS) of PD at an early stage and HN images. The network is trained by 190 images of HN and 430 images of early-stage PD. The selected input is given to the proposed JAN network. The input is processed using five convolutional layers, two Modified ExFeat blocks, and two fully connected layers. The mathematical explanation of each layer is explained in the following section.

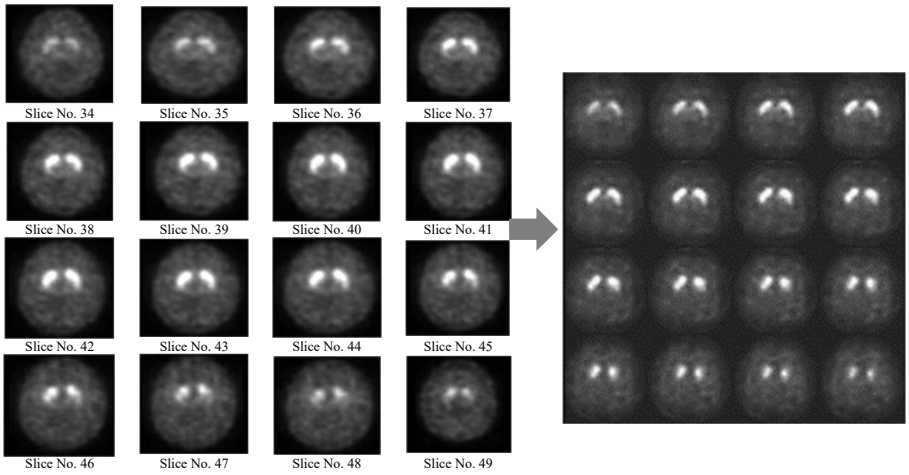

Fig. (1). (**a**) Selected 16 slices from a SPECT image, (**b**) single volume rendering Image slice (VRIS).

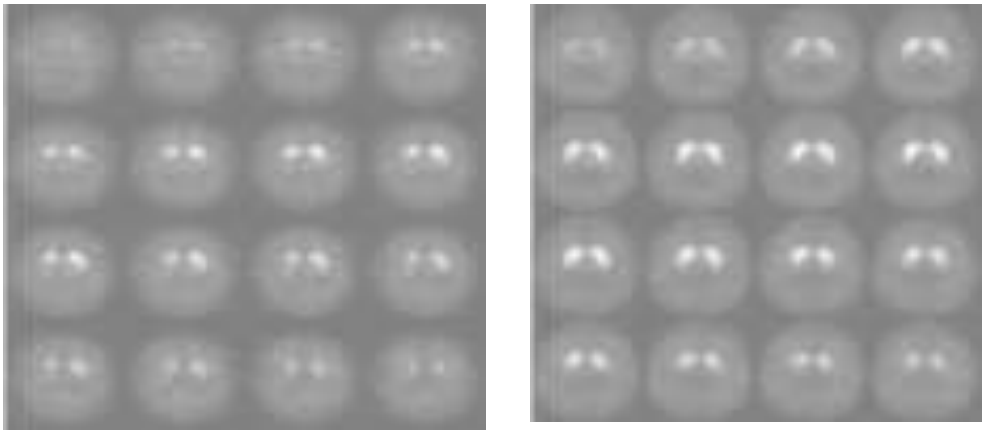

Fig. (2). Volume rendering image slices of (**a**) Early-stage PD, (**b**) Healthy normal.

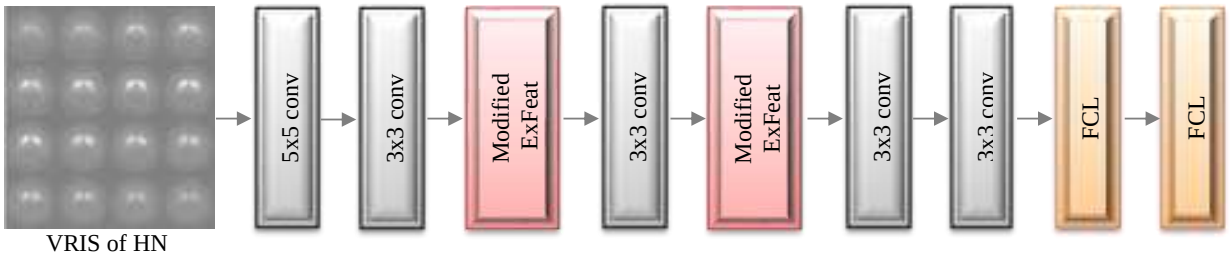

Fig. (3). The proposed JAN network architecture [20].

3.1. Convolutional Layer

The convolutional layer is the first and core block in constructing CNN architecture. It performs a convolutional operation where the filter convolves with an input image and makes an activation map. The mapping is performed by the activation function called ReLU which is a nonlinear function. The details of the convolutional layer are discussed as follows: The convolutional operation is a simple 'dot' product over the input images by applying the filters. Each convolutional layer holds neurons with bias and weights which captures DaT content as a feature from the VRIS. Consider an input image is I(*mxn)* and the convolutional filter represents f_a(pxq), $a \epsilon V$, with a kernel size of *(pxq)*. V represents the depth of the filters. The output of the computed feature map is given as:

$$Z_{conv} = \sum_{x=1}^{p} \sum_{y=1}^{q} f_a(x,y) \;\; I(m-x, n-y)$$

The convolutional layer of the JAN network uses stride 2 for downsampling of the VRIS as an alternative to max pooling. This layer executes cross-correlation operations and preserves all relevant features. The output equation of the stride 2 convolutional layer is given below:

$$Z_{conv/2} = \sum_{x=p/2}^{p/2} \sum_{y=-q/2}^{q/2} f_a(x,y) \;\; I(\alpha - x, \beta - y)$$

where, α= 2m-1, β=2n-1

3.2. Rectified Linear Unit (ReLu)

Rectified linear unit or ReLu is the activation function applied to minimize the backpropagation error in the network. It is also used to find out the non-linear relationship between the pixels of the striatum which is to be learned from linear relationships by applying the monotonic function. The ReLu activation function is used to produce the sparse feature output [19]. The response of ReLu is calculated using the maximum function of the input images and it is given as:

$$Z_{\varphi} = maximum\ (0, I(m,n))$$

The output of the ReLu block is fed into Modified ExFeat which secures all the significant features of VRIS of SPECT images.

3.3. Modified ExFeat block (M- ExFeat)

The Modified ExFeat block (M-ExFeat) is designed from the ExFeat block of the EXPERT net [17]. The Modified ExFeat block consists of only three convolutional layers with one additive layer. The size of the filters is chosen in such a way that the output must extract the edge and position of the striatum accurately. The shape of the striatum is accurately learned by three convolutional layers of JAN Net than four

convolutional layers in EXPERT net which reduces the complexity of the network as well. The convolutional layer is built using filters that have a depth of 32 and sizes of 1x1, 3x3, and 5x5 respectively. All the edge features (micro and macro) of the striatum are extracted by distinct filters of the M-ExFeat block. M-ExFeat block also includes an additive layer to enhance the performance of the network. The additive layer sums up the output of each convolutional layer and provides better decision-making in the shape of the striatum. It improves the learning capability of the hidden layer's neurons. The total outcome of the M-ExFeat block is given below:

$$Z_{M-ExFeat} = Z_{conv\,3a} + Z_{conv\,3b} + Z_{conv\,3c}$$

The detailed structure of the Modified ExFeat (M-ExFeat) block is given in (Fig. **4**). The M-ExFeat incorporates three filters with different sizes (1x1, 3x3, and 5x5) with the same depth (32) and same padding. Padding 'same' yields the same size of input and output. The convolutional layer extracts the pixel values in different levels which is sum up by the additive layer. The output of the additive layer is more accurate than other outputs in the literature. In addition, JAN Net repeats twice the operation of the M-ExFeat block with the same channel depth to improve the learning process of weight and this will be fed into the fully connected layer.

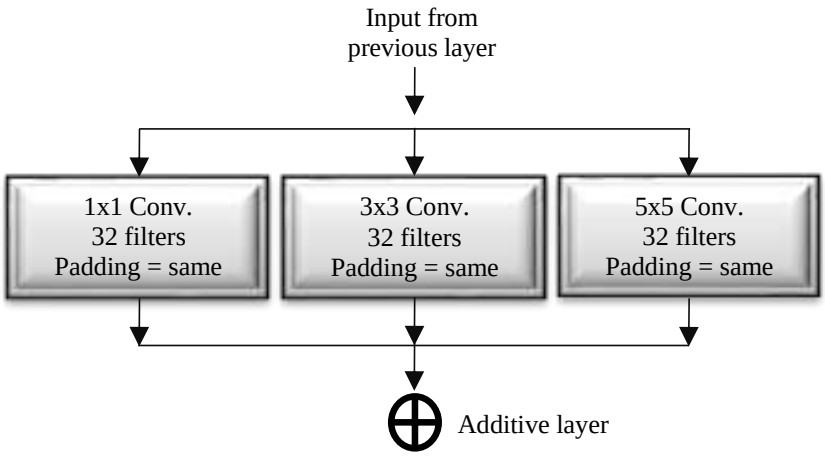

Fig. (4). Structure of the Modified ExFeat network.

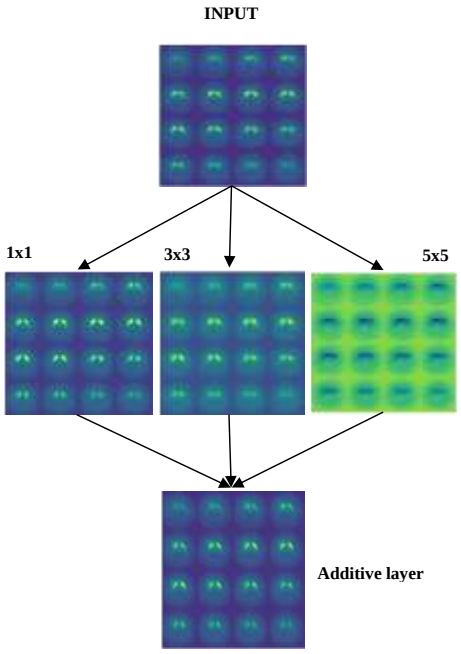

Fig. (5). Input VRIS and its feature maps of the filters 1x1, 3x3, and 5x5 in M-ExFeat block. The output of the additive layer.

Table 1. The Structure of the JAN Net with activations and total learnable parameters.

Name of the Layers		Activations	Learnable	Total Learnable Parameters
Input image		-	-	0
Conv_1 32 Fd, 5x5 Fs [1, 1] S		224x224x32	Weights 5x5x32 Bias 1x1x32	2432
Conv_2 32 Fd, 3x3Fs [1, 1] S		75x75x32	Weights 3x3x32x32 Bias 1x1x32	9248
Modified ExFeat block	**Conv_3a** 32 Fd, 1x1Fs [2, 2] S	75x75x32	Weights 1x1x32x32 Bias 1x1x32	1056
	Conv_3b 32 Fd, 3x3Fs [2, 2] S		Weights 3x3x32x32 Bias 1x1x32	9248
	Conv_3c 32 Fd, 5x5Fs [2, 2] S		Weights 5x5x32x32 Bias 1x1x32	25632
	Addition	75x75x32	-	-
Conv_4 32 Fd, 3x3Fs [2, 2] S		38x38x32	Weights 3x3x32x32 Bias 1x1x32	9248
Modified ExFeat block	**Conv_5a** 32 Fd, 1x1 Fs [2, 2] S	38x38x32	Weights 1x1x32x32 Bias 1x1x32	1056
	Conv_5b 32 Fd, 3x3Fs [2, 2] S		Weights 3x3x32x32 Bias 1x1x32	9248
	Conv_5c 32 Fd, 5x5Fs [2, 2] S		Weights 5x5x32x32 Bias 1x1x32	25632
	Addition	38x38x32	-	-
Conv_6 32 Fd, 3x3Fs [2, 2] S		19x19x32	Weights 3x3x32x32 Bias 1x1x32	9248
Conv_7 32 Fd, 3x3 Fs [4, 4] S		5x5x32	Weights 3x3x32x32 Bias 1x1x32	9248
Fully connected layer (2 outputs)		1x1x2	Weights 2x512 Bias 2x1	1026
Fully connected layer (2 outputs)		1x1x2	Weights 2x2 Bias1x2	1026

Note: Fd: Depth of the filter, Fs: Size of the filter, S: Stride

3.4. Fully Connected Layer (FCL)

FCL is also called multilayer perceptron because it connects all former layer neurons to every neuron of the self-generative layer. The hidden layer input is given as R and the size (number of neurons) is l and N. The activation function of the FCL is estimated using matrix multiplication and the bias is added with it. The general expression of the fully connected layer is given as $\boldsymbol{e_s} = \psi(\boldsymbol{M} * \boldsymbol{z})$

where ψ is called as Activation function

M is resultant matrix of size Nxl.

The detailed structure of the JAN Net is depicted in Table **1**. The Table shows the activations, learnable, and total learning parameters of the proposed JAN network.

3.5. Investigation of the Proposed JAN Architecture

The conventional Alex Net [12], VGG Net [14], and PD Net [23] and their developmental models in the literature are implemented to diagnose PD. In addition to them, motivated by EXPERT Net (that identifies facial expressions), a novel architecture called JAN Net is proposed for identifying early-stage PD which maps the features of the striatum by applying the property of linear cross-correlation and depth of the filter. The depth of the filter improves the learnability of the neuron by regularly updating the filters' weights.

The M-EXFEAT net incorporates filters of sizes 1x1, 3x3, and 5x5 respectively. All these filters extract micro and macro edge features of the striatum. The extracted features are added to fix its shape accurately. The output of the additive layer is shown in (Fig. **5**). This minimizes the computational complexity and improves learnability and computational power, thus improving the discrimination between EPD and HN.

The JAN Net uses stride 2 for the convolutional layer which minimizes the input image size and information loss as depicted in (Fig. **6**) which shows input VRIS and response feature map of stride 1 and stride 2. It is noted from the figure that the stride 2 response feature map improves the discrimination ability more than stride 1. Hence, stride 2 is utilized for further analysis of VRIS using JAN Net. The Visualization of the input and response feature map of early PD and Healthy normal of the JAN for stride 2 is depicted in (Fig. **7**). It is evident from the figure that the shape of the striatum is clearly visible in identifying EPD.

3.6. Comparison of Hoehn and Yahr Scale

The Hoehn and Yahr (H&Y) rating scale is applied to describe the progression of Parkinson's disease. It was first published in the year of 1967 and modified in the year of 2004. The different stages of the scale are given below: Stages 1.0 and 1.5 are related to the problem of one side and the other side with its axis respectively. Stage 2.0 and 2.5 describes the

problem of two-sided without balance problem and with retrieval on the test of postural stability. Stage 3.0 explains slightly modest two-sided problems with some physicallyindependent postural instability. Stage 4.0 deals with severe disability and physically dependent. And stage 5.0 tells the problem of being bedridden or wheelchair-bound. In the proposed work, the first two stages are considered as early stages of the disease as per the guidelines of the PPMI database.

4. RESULTS AND DISCUSSION

4.1. Performance of the Network and its Investigation

The performance of the JAN network is tested by the VRIS of SPECT images taken from the PPMI database. The output of the network is validated using 10 epochs. Here, input VRIS were divided into 70:30 ratios for training and testing respectively. The accuracy of the network is calculated by the equation:

$$\text{Accuracy} = \frac{Number\ of\ correctly\ predicted\ data}{Total\ number\ of\ samples} \text{x } 100$$

JAN network is trained using various hyperparameters. The network parameter is selected in such a way that the JAN Net offers better performance in identifying early Parkinson's disease. The selected hyperparameter is given in Table **2**. The network is trained using the Deep learning designer toolbox of Matlab 2021a.

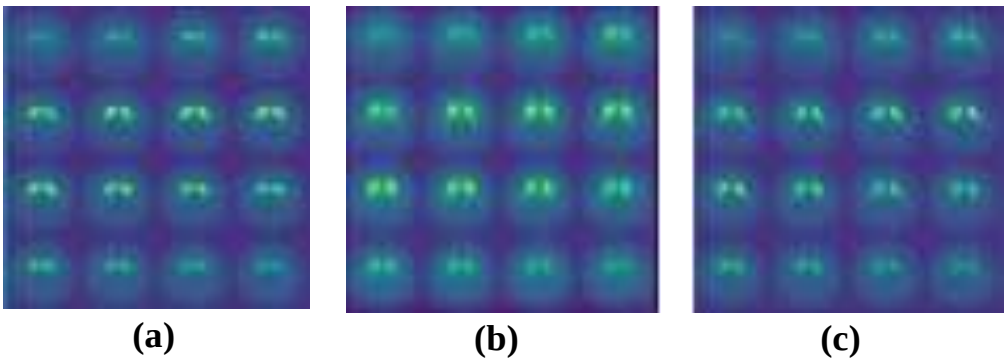

Fig. (6). Input image (**a**) and the response image by applying convolution layer with (**b**) stride 1 and (**c**) stride 2.

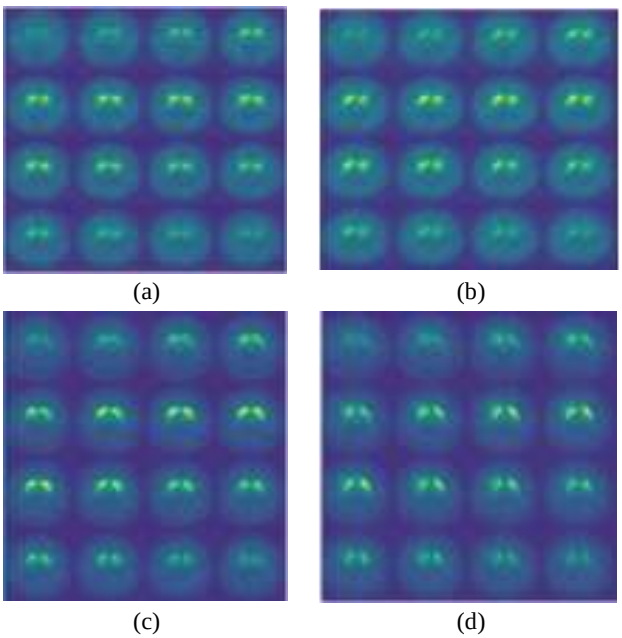

Fig. (7). Visualization of input and response feature map of early PD (**a**, **b**) and Healthy normal (**c**, **d**).

Table 2. Hyperparameter of the JAN Net.

S. No.	Hyperparameter	Value
1.	Optimizer	Adam
2.	Initial learning rate	0.001
3.	Epoch	10
4.	Iterations per epoch	14
5.	Sequence padding value	0

Table 3. Performance metrics for original data of JAN Net.

Epoch	Stride 1			Stride 2
-	Training Accuracy	Validation Accuracy	Training Accuracy	Validation Accuracy
1	100.0	58.4	13.0	100.0
2	76.0	66.8	44.2	96.8
3	82.0	76.8	50.0	96.8
4	91.0	86.8	69.0	98.4
5	94.0	88.4	89.0	96.8
6	93.0	91.5	90.0	98.4
7	95.7	92.9	92.9	96.8
8	93.0	94.4	93.2	96.8
9	93.8	95.2	92.4	93.4
10	93.8	95.4	92.4	96.1
Overall	93.8	95.4	92.4	96.1

The performance metric of the original data (without augmentation) for stride 1 and stride 2 is compared in Table **3**. It is noted from the table that the validation accuracy for stride 1 and stride 2 is 95.4% and 96.1% respectively. The network uses different strides for analyzing the performance and computational complexity of the network. In order to enhance the network performance further, data augmentation is introduced.

Data augmentation is also performed to formulate a dataset huge in size and to reduce overfitting. The augmentation is done by translating the image randomly ranging from 1, 5 for x and y axis (vertical and horizontal). The augmented data are tested for both stride 1 and stride 2 networks. Table **4** shows the performance of the JAN network that includes epochs, training accuracy, validation accuracy, and its losses for both strides 1 and 2. The overall accuracy of training and testing is given as 100%, 99.37% for stride 1 and 100%, and 100% for stride 2. The highest accuracy portrays that the JAN Net with stride 2 performed well for VRIS of SPECT image in diag nosing early PD. Moreover, minimum losses of the network indicate that the network creates a more precise generalization model for the input data. The losses given in the table are negligible when compared with the accuracy of the network.

It can be concluded from the Table **3** and **4**, the network offers better performance for augmented data in stride 2 than the original data. The huge amount of data reduces overfitting and gives a significant accuracy in detecting early PD. The accuracy and losses of training, and validation datasets for stride 2 are also plotted in (Fig. **8**). The losses are the summation of errors in the JAN network. The less are losses and errors, the best the model classifies. The line graph confirms that the stride 2 training and validation accuracy is higher than stride 1 for every epoch. The losses of training and validation are 0.0001, 0.0478 for stride 1 and 2.2577e-05, and 8.9375e-05 for stride 2 respectively. The accuracy and losses confirm that the model is highly fitting with the data to eliminate the problem of overfitting. To summarize, the parallel network offers better performance in discriminating EPD from HN than serial networks. Table **5** gives the average classification accuracy of serial and parallel networks for stride 1 and stride 2 wherein stride 2 parallel network classifies the subjects 100% accurately.

Table **6** depicts the comparative analysis of the classification accuracy of the network in the literature with the proposed network. Comparing the present work with other works, it is evident that the present work gives the highest accuracy in classifying EPD from HN. The related works also report the close outcome of the proposed work; yet, it differs from the architectural design, parameter used, and size of the dataset. Hence, the proposed work offers the highest and bias-free output than the related works. A comparison of architectural design and computational complexity is discussed in detail in the following section.

4.2. Computational Complexity

The computational complexity of the JAN Net is compared with existing networks. The JAN Net has only 1M as the highest learnable parameter which is a lesser amount as compared with the existing networks like VGG-16, VGG-19, GoogleNet, ResNet, and EXPERT Net which have 138M, 144M, 4M, 11M, and 4M respectively. Moreover, the depth of the channels and the hidden layers of the JAN Net is less than the former methods. It is noticeable that JAN Net comprises 09 layers whereas VGG-16 is 16, VGG-19 is 19, GoogleNet is 22 and ResNet is 34 and EXPERT Net is 13 layers respectively [12, 13, 15, 20].

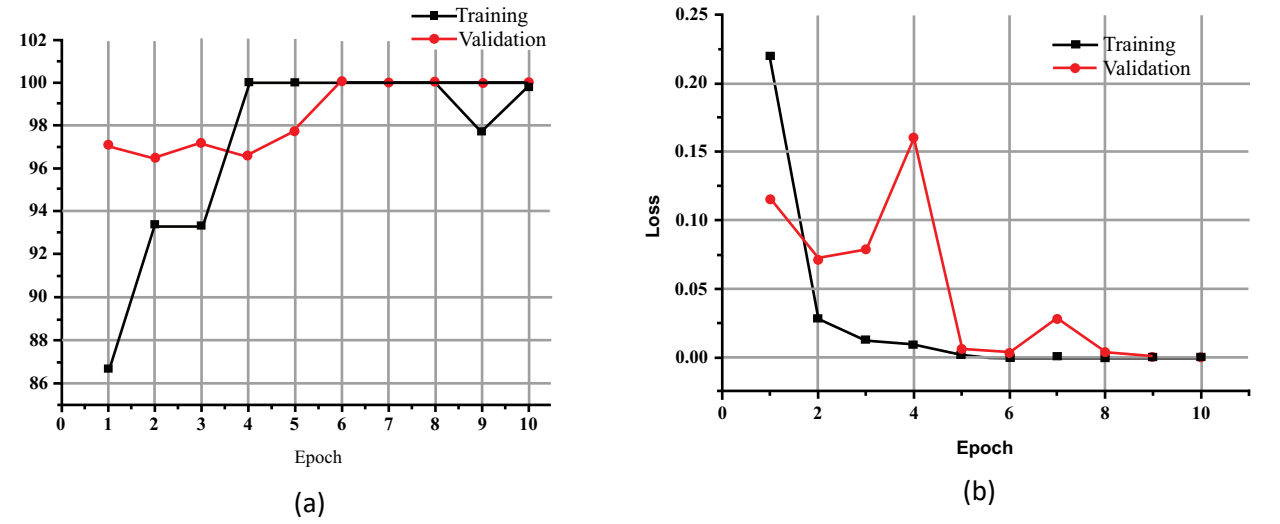

Fig. (8). The (**a**) accuracy and (**b**) losses of the JAN Net for stride 2.

Table 4. Performance metrics for augmented data of JAN Net.

Epoch	Stride 1				Stride 2			
	Accuracy		Loss		Accuracy		Loss	
-	Training	Validation	Training	Validation	Training	Validation	Training	Validation
1	29.69	68.61	10.9000	5.0000	86.67	97.09	0.2198	0.1155
2	89.84	87.59	1.3200	1.4100	93.37	96.46	0.0284	0.0712
3	95.31	96.96	0.1044	0.1849	93.33	97.22	0.0122	0.0788
4	96.09	65.82	0.1393	0.2286	100.00	96.58	0.0093	0.1601
5	100.00	98.35	0.0060	0.1440	100.00	97.72	0.0014	0.0060
6	100.00	99.86	0.0001	0.1175	100.00	100.00	0.0004	0.0033
7	100.00	99.37	0.0058	0.1038	100.00	100.00	0.0003	0.0281
8	100.00	99.37	0.0000	0.0957	100.00	100.00	0.0005	0.0037
9	100.00	99.37	0.0044	0.0735	97.76	100.00	0.0002	0.0003
10	100.00	99.37	0.0001	0.0478	99.90	100.00	0.0001	0.0001
Overall	100.00	99.37	0.0001	0.0478	100.00	100.00	2.2577e-05	8.9375e-05

Table 5. Calculated accuracy of various network.

S. No.	Network Implemented	Accuracy (%)
1	Parallel network for stride 1	100
2	Parallel network for stride 2	96.10
3	Serial network for stride 1	86.36
4	Serial network for stride 2	93.94

Table 6. Calculated accuracy of the related work.

S. No.	Methodology	Accuracy in %
1	Ordinal graph-based oversampling via shortest paths- beta (OGO-SP-β) [22]	88.19
2	PD Net [23]	98.8
3	Deep PD net [24]	96.71
4	Deep PD net+ batch Normalization [24]	96.87
5	3D CNN [25]	70.60
6	DaTNet-3 [26]	98.5

(Table 6) contd.....

S. No.	Methodology	Accuracy in %
7	3D CNN [27]	99.34
8	RA and ANN [28]	93.46
9	Transfer Alex Net [29]	89.23
10	Extreme learning machine (Machine learning algorithm for 16 VRIS) [10]	99.3
11	Artificial neural network (Machine learning algorithm for 16 VRIS) [10]	98.3
12	Proposed JAN Net (CNN for 16 VRIS)	100

CONCLUSION

An effective CNN architecture, called JAN Net is specifically designed for Volume rendering image slices (VRIS) of 3D SPECT images to diagnose early Parkinson's disease. The network consists of a convolutional layer, a modified exigent feature (M-ExFeat) block, and a fully connected layer. The M-ExFeat block integrates 4 convolutional layers with an additive layer which enhances the capability of preserving the edge features of the striatum. The additive layer sums up the response of all convolutional layers (filter size of 1x1, 3x3, 5x5) to enhance the performance of the network. The stride 1 and 2 networks are tested to achieve better performance for the original as well as the augmented data. The evaluated performance of the JAN Net for stride 2 is given the highest training and validation accuracy of 100%, and 100% and the lowest training and validation losses of 2.2577e-05, and 8.9375e-05 respectively. Thus, the network results have evidenced the efficiency of the proposed JAN Network.

LIST OF ABBREVIATIONS

PD = Parkinson's Deepisease

SPECT = Single-photon Emission Computed Tomography

CNN = Convolutional Neural Network

PPMI = Parkinson's Progression Markers Initiative

ETHICS APPROVAL AND CONSENT TO PARTICIPATE

Not applicable.

HUMAN AND ANIMAL RIGHTS

No Animals/Humans were used for studies that are base of this research.

CONSENT FOR PUBLICATION

Not applicable.

CONFLICT OF INTEREST

The authors declare no conflict of interest, financial or otherwise.

ACKNOWLEDGEMENTS

PPMI - a public-private partnership - is funded by the Michael J. Fox Foundation for Parkinson's Research and funding partners, including [list of all of the PPMI funding partners found at www.ppmi-info.org/fundingpartners].

REFERENCES

[1] de Lau LML, Breteler MMB. Epidemiology of Parkinson's disease. Lancet Neurol 2006; 5(6): 525-35. [http://dx.doi.org/10.1016/S1474-4422(06)70471-9] [PMID: 16713924]

[2] DeMaagd G, Philip A. Parkinson's disease and its management: Part 1: Disease entity, risk factors, pathophysiology, clinical presentation, and diagnosis. P T 2015; 40(8): 504-32. [PMID: 26236139]

[3] Pringsheim T, Jette N, Frolkis A, Steeves TDL. The prevalence of Parkinson's disease: A systematic review and meta-analysis. Mov Disord 2014; 29(13): 1583-90. [http://dx.doi.org/10.1002/mds.25945] [PMID: 24976103]

[4] Armstrong MJ, Okun MS. Diagnosis and treatment of Parkinson disease: A review. JAMA 2020; 323(6): 548-60. [http://dx.doi.org/10.1001/jama.2019.22360] [PMID: 32044947]

[5] Ball N, Teo WP, Chandra S, Chapman J. Parkinson's disease and the environment. Front Neurol 2019; 10: 218. [http://dx.doi.org/10.3389/fneur.2019.00218] [PMID: 30941085]

[6] Korolev S, Safiullin A, Belyaev M, Dodonova Y. Residual and plain convolutional neural networks for 3D brain MRI classification. IEEE International Symposium on Biomedical Imaging. Melbourne, VIC, Australia, 18-21 April 2017, pp.835-838. [http://dx.doi.org/10.1109/ISBI.2017.7950647]

[7] Marek K, Jennings D, Lasch S, *et al.* The Parkinson Progression Marker Initiative (PPMI). Prog Neurobiol 2011; 95(4): 629-35. [http://dx.doi.org/10.1016/j.pneurobio.2011.09.005] [PMID: 21930184]

[8] Prashanth R, Dutta Roy S, Ghosh S, Pravat Mandal K. Shape features as biomarkers in early Parkinson's disease. 6th International IEEE/EMBS Conference on Neural Engineering (NER). San Diego, CA, US, 06-08 November 2014.

[9] Francisco PMO, Castelo-Branco M. Computer-aided diagnosis of Parkinson's disease based on [123I] FP-CIT SPECT binding potential images, using the voxels-as-features approach and support vector. J Neural Eng 2015; 12: 10.

[10] Anita S, Aruna Priya P. Diagnosis of parkinson's disease at an early stage using volume rendering spect image slices. Arab J Sci Eng 2020; 45(4): 2799-811. [http://dx.doi.org/10.1007/s13369-019-04152-7]

[11] Anita S, Priya PA. Three dimensional analysis of SPECT Images for diagnosing early Parkinson's disease using radial basis function kernel − Extreme learning machine. Curr Med Imaging Rev 2019; 15(5): 461-70. [http://dx.doi.org/10.2174/1573405614666171219154154] [PMID: 32008553]

[12] Krizhevsky A, Suskever I, Hinton GE. ImageNet classification with deep convolutional neural networks. Adv Neural Inf Process Syst 2012; 25: 1097-105.

[13] LeCun Y, Bengio Y, Hinton G. Deep learning. Nature 2015; 521(7553): 436-44. [http://dx.doi.org/10.1038/nature14539] [PMID: 26017442]

[14] Simonyan K, Zisserman A. Very deep convolutional networks for large-scale image recognition. arXiv 2014; 2014: 1556.

[15] He K, Zhang X, Ren S, Sun J. Deep residual learning for image recognition. IEEE conference on computer vision and pattern recognition. Las Vegas, NV, USA, 27-30 June 2016, pp.770-778. [http://dx.doi.org/10.1109/CVPR.2016.90]

[16] Szegedy C, Vanhoucke V, Ioffe S, Shlens J, Wojna Z. Rethinking the inception architecture for computer vision. IEEE conference on computer vision and pattern recognition. Las Vegas, NV, USA, 27-30 June 2016, pp.2818-2826. [http://dx.doi.org/10.1109/CVPR.2016.308]

[17] Ortiz A, Munilla J, Martínez-Ibañez M, Górriz JM, Ramírez J, Salas-Gonzalez D. Parkinson's disease detection using isosurfaces-based

features and convolutional neural networks. Front Neuroinform 2019; 13: 48.
[http://dx.doi.org/10.3389/fninf.2019.00048] [PMID: 31312131]

[18] The study that could change everything. 2010. Available From: https://www.ppmi-info.org

[19] Gil-Martín M, Montero JM, San-Segundo R. Parkinson's disease detection from drawing movements using convolutional neural networks. electronics 2019; 8(8): 907.
[http://dx.doi.org/10.3390/electronics8080907]

[20] Verma M, Bhui JK, Vipparthi SK, Singh G. EXPERTNet: Exigent features preservative network for facial expression recognition. 11th Indian Conference on Computer Vision, Graphics and Image Processing (ICVGIP 2018). New York, NY, USA. 2018; pp. 1-8.
[http://dx.doi.org/10.1145/3293353.3293374]

[21] Masood S, Sharif M, Masood A, Yasmin M, Raza M. A survey on medical image segmentation. Curr Med Imaging Rev 2015; 11(1): 3-14.
[http://dx.doi.org/10.2174/1573405611011504231034 41]

[22] Djang DSW, Janssen MJR, Bohnen N, *et al.* SNM practice guideline for dopamine transporter imaging with 123I-ioflupane SPECT 1.0. J Nucl Med 2012; 53(1): 154-63.
[http://dx.doi.org/10.2967/jnumed.111.100784] [PMID: 22159160]

[23] Barbero-Gómez J, Gutiérrez P-A, Vargas V-M, Vallejo-Casas J-A, Hervás-Martínez C. An ordinal CNN approach for the assessment of neurological damage in Parkinson's disease patients. Expert Syst Appl 2021; 182: 115271.
[http://dx.doi.org/10.1016/j.eswa.2021.115271]

[24] Choi H, Ha S, Im HJ, Paek SH, Lee DS. Refining diagnosis of Parkinson's disease with deep learning-based interpretation of dopamine transporter imaging. Neuroimage Clin 2017; 16: 586-94.
[http://dx.doi.org/10.1016/j.nicl.2017.09.010] [PMID: 28971009]

[25] Pianpanit T, Lolak S, Sawangjai P, Sudhawiyangkul T, Wilaiprasitporn T. Parkinson's disease recognition using SPECT image and interpretable AI: A tutorial. IEEE Sensors J 2021; 99

[26] Nikhil JD, Thomopoulos SI, Owens-Walton C, *et al.* 3D Convolutional neural networks for classification of Alzheimer's and Parkinson's disease with T1-weighted brain MRI. bioRxiv 2021; 2021: 453903.
[http://dx.doi.org/https://doi.org/10.1101/2021.07.26.453903]

[27] Wolfswinkel Ev, Wielaard J, Lavalaye J. Artificial intelligence-based assistance in clinical 123I-FP-CIT SPECT scan interpretation. Res Square 2021.
[http://dx.doi.org/10.21203/rs.3.rs-721186/v1]

[28] Mohammed F, He X, Lin Y. Retracted: An easy-to-use deep-learning model for highly accurate diagnosis of Parkinson's disease using SPECT images. Comput Med Imaging Graph 2021; 87: 101810.
[http://dx.doi.org/10.1016/j.compmedimag.2020.101810] [PMID: 33279760]